Applied Mathematical Modelling ••• (••••) •••–•••

Contents lists available at ScienceDirect

Applied Mathematical Modelling

journal homepage: www.elsevier.com/locate/apm

Mastering the art: Proficient finite element implementation and robust evaluation of a strain-hardening porous ductile material crack growth prediction model at finite strain

Koffi Enakoutsa, Yuelian Li

Department of Mathematics, University of California, Los Angeles, Los Angeles, CA, 90095-1555, United States of America

A B S T R A C T

Accurate prediction of crack extension is crucial for ensuring the structural integrity of metal components exposed to diverse loads. While the Gurson model and its extensions are widely accepted for delineating ductile fracture stages, especially in porous materials with a rigid-perfectly plastic matrix, their efficacy diminishes in the presence of strain-hardening matrices. To address this limitation, our study introduces a robust numerical implementation and assessment of Perrin's model. In contrast to Gurson's approach, Perrin's model incorporates two distinct strain-hardening parameters derived from an intricate analysis of a strain-hardening hollow sphere subjected to axisymmetric loading.

Moving beyond theoretical discussions, this paper actively engages in the rigorous evaluation of Perrin's model under various scenarios, encompassing isotropic, kinematic, and mixed isotropic-kinematic hardening conditions. The model's effectiveness is convincingly demonstrated through meticulous comparisons between numerical simulations and real-world experimental observations conducted on pre-cracked specimens.

Facing challenges related to achieving global elastic-plastic convergence in large-scale simulations, our research introduces a sophisticated approach. Leveraging stiffness tangent moduli ensure the maintenance of quadratic convergence in global Newton method iterations. This not only enhances the reliability of our simulations but also underscores the practical applicability of our findings.

The study also focuses on the necking and crack propagation of a cylindrical specimen through meticulous computational modeling. Our mesh captures intricate details and addresses stress gradients, revealing coplanar crack propagation contrary to prior beliefs. The confirmation of the cup-cone fracture effect challenges previous interpretations, emphasizing the critical role of void nucleation. This reinforces the credibility and applicability of our approach in advancing the understanding of material fracture behavior.

In summary, this study significantly contributes to existing knowledge in fracture prediction models, offering a robust framework for predicting ductile fracture under substantial deformations. The presented findings pave the way for advancements in structural engineering, providing invaluable insights for optimizing the performance and resilience of metal structures in real-world applications.

1. Introduction

The integrity of engineering metal structures subjected to dynamic, cyclic, or quasi-static loads necessitates a comprehensive investigation of crack initiation and propagation. However, the primary challenge lies in finding a predictive tool capable of not only identifying crack initiation but also accurately predicting the subsequent crack extension. In the realm of ductile fracture, which stands as the predominant failure mode in metals under both room and high-temperature conditions, the micro-mechanically based model proposed by Gurson [1], along with its heuristic extensions by Tvergaard [2] and Tvergaard and Needleman [3], has gained widespread acceptance for describing the three successive stages of ductile fracture: cavity nucleation, growth, and coalescence.

E-mail address: koffi@math.ucla.edu (K. Enakoutsa).

https://doi.org/10.1016/j.apm.2024.04.035
Received 17 September 2023; Received in revised form 6 April 2024; Accepted 16 April 2024

0307-904X/© 2024 Elsevier Inc. All rights reserved.

Please cite this article as: K. Enakoutsa and Y. Li, Mastering the art: Proficient finite element implementation and robust evaluation of a strain-hardening porous ductile material crack growth prediction model at finite strain, Applied Mathematical Modelling, https://doi.org/10.1016/j.apm.2024.04.035

Nomenclature

α	A dimensionless parameter in the nucleation model	Θ	The angle of rotation
δ	Coalescence's accelerating factor	Σ_{eq}	The equivalent stress
λ	A Lame's coefficient	f	The porosity
$\mathbf{B}$	Strain-displacement tensor	f_0	The initial porosity
α	Tensor representing the center of the domain of elasticity	f_c	Critical porosity at the onset of coalescence
$\mathbf{\Sigma}$	Cauchy stress tensor	l	The characteristic length scale in the nonlocal model
$\mathbf{d}^{\mathrm{e}}$	The elastic part of the strain	q	Cavities's interaction parameter
$\mathbf{d}^{\mathrm{p}}$	The plastic part of the strain	R	Current radius of the cavity in the Rousselier model
$\mathcal{V}$	The volume	R_0	Initial radius of the cavity in the Rousselier model
A	Nucleation model parameter	T	The initial triaxiality
Rez	Vector representing the nodal forces	TOL	Convergence precision
$\hat{\mathrm{F}}_e$	External nodal forces	E	The Young's Modulus
$\hat{\mathrm{F}}_i$	Internal nodal forces	Ω	The rotation tensor
μ	A Lame's coefficient	$\mathbf{d}$	Deformation rate tensor
ϕ	Angle involved in the parametrization of the yield criterion	ΔE	Rate of change for the Young's Modulus due to temperature change
ρ	Proportion of kinematics hardening	$\dot{f}_{cl}$	The local rate of increase of porosity by growth
Σ_1	Hardening parameter in the LPD model	$\dot{f}_{gl}$	The local rates of increase of porosity by nucleation
Σ_2	Hardening parameter in the LPD model		
Σ_0	The stress yield limit (independent of the temperature)	$\hat{\mathbf{\Sigma}}$	Objective derivative of Cauchy stress tensor
		$\mathbf{\Phi}$	Gurson yield function
Σ_c	The critical stress in the nucleation model	ϕ	The function defining the modified Gurson's yield criterion
Σ_I	The greatest principal stress of the stress tensor		
Σ_y	The initial yield strength in uniaxial tension	Σ_{eq}	The equivalent stress
$\mathfrak{R}$	Residual vector to test convergence	θ	The temperature

Numerous studies have demonstrated the effectiveness of the Gurson model in characterizing crack propagation in pre-cracked metal structures, as well as in small uncracked laboratory test samples like smooth and notched round tensile specimens or plane strain specimens. Notably, the works of [3], [4], [5] have provided compelling evidence of the Gurson model's efficacy in accurately predicting the phenomenon known as "cup-cone" fracture in smooth axisymmetric tensile specimens. This phenomenon is characterized by the initial radial propagation of the crack from the axis, followed by a subsequent deviation at approximately a 45° angle from the plane when it nears the cylindrical free surface.

An extension of the Gurson model [1] developed some years ago by Perrin [6], presents a certain number of theoretical improvements compared to the model "R/R_0" and Rousselier's damage model [7]:

- better consideration of the interactions between the growth of cavities and hardening, and the introduction of the possibility of kinematic or mixed isotropic $\diagup$ kinematic hardening;
- better modeling of coalescence;
- taking into account the nucleation, brutal or continuous, of the cavities, which can allow for the simulation of the behavior of specimens in stainless steel aged by irradiation for instance;
- incorporation of damage delocalization into the model itself, not just through the imposition of a minimum mesh size. This makes it possible to overcome the usual restrictions on the shape and size of the meshes.

In addition, the experience has revealed other advantages of Perrin's model and/or its numerical implementation, of a more computational nature:

- The model accommodates square meshes, unlike that of Rousselier's damage model [7], which required the use of elongated rectangular meshes forcing the crack to remain in its plane. This made it possible to simulate the "cup-cone fracture" experiment, in which the crack deviates at 45° from its initial path.[1]
- The model adequately reproduces the behavior of homothetic test specimens of small dimensions, a result which could not be obtained until now. The precise origin of this improvement, however, is unclear.

[1] The coalescence, neglected in the model of Rousselier's damage model [7], is only taken into account in a relatively coarse way in the model "R/R_0", because of the absence of coupling plasticity damage.

In the realm of crack propagation, it is common for the process to occur in areas of the materials where strain and damage concentrate. These localized regions exhibit incredibly steep stress and damage gradients, leading to a significant reliance on the mesh size used in finite element (FE) computations. As the mesh size becomes finer, a peculiar phenomenon arises: damage and strain tend to concentrate within zero-width bands. This intricate issue is widely acknowledged when attempting to model the response of ductile materials. The challenge arises from the need for more precise data regarding both deformation and stress states in the post-localization regime of these materials.

A proposal to circumvent this drawback was presented by Enakoutsa and co-workers [8], [9], and [10]. Their proposal consists of adding, following an earlier suggestion by Pijaudier-Cabot and Bazant [11], a characteristic length scale to the constitutive model. This addition is accomplished through the convolution of the damage evolution equation with a carefully chosen weight function. Referred to as the "damage delocalization technique," this approach has effectively eradicated the detrimental influence of mesh size variations in finite element computations related to problems associated with ductile fracture. This accomplishment has been acknowledged by many researchers such as Leblond et al. [12], Tvergaard and Needleman [13] and [14], Enakoutsa [9], and Enakoutsa et al. [8].

Leblond et al. [12] proposed a heuristic approach, which unfortunately lacked a solid theoretical foundation. This limitation prompted Gologanu et al. [15] to develop a more comprehensive and physically-based alternative. In their work, Gologanu and colleagues derived an enhanced version of Gurson's model, known as the GLPD model, by refining the original homogenization procedure based on the classical conditions of homogeneous boundary strain rate outlined by Mandel [16] and Hill [17]. Gologanu et al. [15] introduced a quadratic relationship between the boundary velocity and the coordinates, aiming to account for the potential rapid variations of macroscopic strain rate encountered during strain localization over short distances comparable to the size of the elementary cell under consideration. The outcome of their homogenization procedure yielded a "micromorphic" model featuring the second gradient of the macroscopic velocity, generalized macroscopic stresses of "moment" type (a product of stress and distance), and a "micro-structural distance" associated with the average spacing between adjacent voids.

Other regularization techniques based on algorithms have been explored, see the work of Areias et al. [18]. This particular methodology employs a staggered algorithm for strain regularization, incorporating the screened Poisson equation. This approach shares similarities with implicit gradient models, often yielding outcomes comparable to those achieved through the widely recognized phase-field theory. To ensure both a reasonable solution and an accurate depiction of crack paths, the method integrates local remeshing. The staggered methodology encompasses a comprehensive set of techniques, including constrained equilibrium analysis, application of the screened Poisson equation, crack detection, recursive local remeshing, node repositioning, and variable transfer, contributing to a robust and versatile framework in the field. Also, another computation-based regularization can be found in the work of Areias et al. [19], which introduces a novel algorithm for Finite Element Method (FEM)-based computational fracture in various materials. The proposed approach, centered on edge rotations, utilizes crack front edges or nodes in surface discretizations as rotation axes. Each rotated edge influences the position of only one or two nodes, minimizing differences between predicted crack paths and edge/face orientations. Unlike remeshing or enrichment, the algorithm focuses on retaining existing entity relations, offering algorithmic and generality advantages. The simplicity of the propagation algorithm, along with its independence from the underlying element used for discretization, sets it apart from alternative methods, making it particularly suitable for history-dependent materials.

The Gurson plasticity criterion is commonly regarded as capable of describing the yield strength of a porous material (containing spherical-shaped voids) with a rigid-perfectly plastic matrix that follows the Von Mises yield criterion. In the case of a strain-hardening matrix, Gurson [1] suggests summarizing the true strain-hardening behavior into a single parameter. This involves replacing the highly heterogeneous true strain-hardening, observed at the microscopic scale, with an "equivalent" homogeneous strain-hardening behavior. This approach has some flaws. Indeed, the classical, precise solution to the hydrostatic loading problem of a hollow rigid-hardenable sphere was not compatible with the phenomenological model. Additionally, the previous prediction that the porosity curve, which represents the relationship between porosity and equivalent strain for a fixed triaxiality during any loading path, solely depended on the initial porosity and triaxiality, but not on the hardening exponent, was found to be incorrect. To address these challenges, Perrin [6] proposed a new model, which tackles the issues by utilizing an approximate analysis of a hollow rigid-hardenable sphere subjected to axisymmetric loading. Two types of strain-hardening parameters are introduced into Gurson's model [1]. These parameters are determined through an approximate solution to the problem of an axisymmetrically deformed strain-hardening hollow sphere.

The objective of this paper is to discuss the numerical implementation and evaluation of the hardening model proposed by Perrin [6]. For the numerical implementation, we shall consider three different cases: isotropic hardening, kinematic hardening, and mixed isotropic-kinematic hardening. For each case, we will address the "problem of projection," which involves adjusting the elastically computed stress tensor to align with the yield locus (plastic correction of the elastic predictor). It is worth noting that the isotropic hardening case has been previously discussed by Enakoutsa [9] and Enakoutsa et al. [8]. Therefore, only a few elements of the projection problem will be presented in this context. We account for large deformation by using the Green-Naghdi derivative for the rates of the stress and the kinematics hardening tensor. We provide the numerical implementation of this derivative in the context of our finite element modeling. Also, because global elasto-plastic iterations might face convergence difficulties, stiffness tangent moduli are derived for maintaining quadratic convergence in global Newton iterations. The assessment of the model will consist of comparing the experimental and numerical results for typical ductile fracture tests.

The paper is organized as follows:

- Section 2 provides a brief description of the theoretical equations of Perrin model [6] including the isotropic, kinematics, and the mixed isotropic-kinematics hardening.
- Next, Section 3 discusses the numerical implementation of the model. The correction of the stress in "the projection problem "for the three types of hardening is discussed.
- Next, Section 4 presents the numerical integration strategy for the case of large deformations and rotations where the deformation of a structure is significant and cannot be accurately approximated using the small displacement theory.
- Finally, in Section 5, the results of some numerical simulations comparing the fracture of a typical axisymmetric pre-cracked specimen to experimental observations reported by Rousselier and Mudry [20] are discussed. Given the challenges in achieving global elastic-plastic convergence for these large-scale simulations, an approach involving stiffness tangent moduli was employed. The objective of this approach is to maintain quadratic convergence in global Newton's iterations. Also, this section exemplifies the robustness of our proposed approach by rigorously investigating the necking and crack propagation of a cylindrical specimen through meticulous computational modeling. Our strategically designed mesh, adept at capturing intricate details and addressing stress gradient challenges, delivers unprecedented insights. Contrary to previous beliefs of zig-zag patterns, our simulations reveal a consistent coplanar crack propagation. The unequivocal confirmation of the cup-cone fracture effect, particularly in simulations involving void nucleation, challenges and reshapes previous interpretations. This study emphatically emphasizes the critical role of considering void nucleation for an accurate portrayal of crack propagation dynamics, reinforcing the credibility and applicability of our approach in advancing the understanding of material fracture behavior.

2. Theoretical equations of the LPD model

The model is written in large deformations, in Eulerian formulation, the deformation rate $\mathbf{d}$ is supposed to admit the usual additive decomposition:

$$\mathbf{d} = \mathbf{d}^{\mathrm{e}} + \mathbf{d}^{\mathrm{p}} \tag{1}$$

The model equations include the expression of the elastic strain rate $\mathbf{d}^{\mathrm{e}}$, that of the plastic strain rate $\mathbf{d}^{\mathrm{p}}$ (plasticity criterion and associated flow rule); and the expressions for the evolution equations for the internal parameters (porosity and hardening parameters).

2.1. Elastic strain rate

The law of elasticity used is in fact (as usual in elasto-plasticity large deformations) a law of hypo-elasticity or weak elasticity (linear relation between the rate of stress and the rate of elastic deformation; it is written, at constant temperature:

$$\hat{\boldsymbol{\Sigma}} = \lambda \left(\mathrm{tr}\mathbf{d}^{\mathrm{e}}\right) \mathrm{I} + 2\mu \mathbf{d}^{\mathrm{e}} \tag{2}$$

where λ and μ denote the Lamé coefficients and $\hat{\boldsymbol{\Sigma}}$ an objective derivative of the stress tensor $\boldsymbol{\Sigma}$. In practice, two derivatives are used: that of Jaumann, defined by:

$$\hat{\boldsymbol{\Sigma}} = \dot{\boldsymbol{\Sigma}} + \boldsymbol{\Sigma} \cdot \boldsymbol{\Omega} - \boldsymbol{\Omega} \cdot \boldsymbol{\Sigma} \tag{3}$$

where $\boldsymbol{\Omega} = \frac{1}{2}\left(\nabla_{\mathrm{x}} \mathrm{U} - {}^{t}\nabla_{\mathbf{x}} \mathrm{U}\right)$ (x current position vector, U velocity vector) denotes the rate of rotation, and that of Green-Naghdi, defined by the same formula Eq. (3), but $\boldsymbol{\Omega}$ then being equal to $\mathbf{R}.\mathbf{R}^{-1}$ where $\mathbf{R}$ is the rotation involved in the polar decomposition of the deformation gradient.

It should be noted that this model does not incorporate a damage-elasticity coupling (λ and μ do not depend on the porosity and are therefore constant if the temperature is), much less important in practice than the damage-plasticity coupling. In the case where the temperature θ varies, we add to the expression of Σ a term proportional to $\dot{\theta}$:

$$\hat{\boldsymbol{\Sigma}} = \lambda \left(\mathrm{tr}\mathbf{d}^{\mathrm{e}}\right) \mathbf{I} + 2\mu \mathbf{d}^{\mathrm{e}} + \frac{\mathrm{dE}}{\mathrm{Ed}\theta} \boldsymbol{\Sigma} \dot{\theta}, \tag{4}$$

where E denotes the Young's modulus. This formula implicitly assumes a temperature-independent Poisson's ratio. It is recalled that it ensures the cancellation of the stresses at high temperatures, and is reduced after integration with the traditional formula

$$\boldsymbol{\Sigma} = \lambda(\theta) \left(\mathrm{tr}\mathbf{d}^{\mathrm{e}}\right) \mathbf{I} + 2\mu(\theta) \mathbf{d}^{\mathrm{e}} \tag{5}$$

in the case where small deformation assumptions are made.

2.2. Plastic strain rate

Let us first consider the case of an isotropic work hardening. The criterion of plasticity is written as:

$$\boldsymbol{\Phi}(\boldsymbol{\Sigma}) = \frac{\Sigma_{\mathrm{eq}}^2}{\Sigma_{\mathrm{l}}^2} + 2p \cosh\left(\frac{3}{2}\frac{\Sigma_{\mathrm{m}}}{\Sigma_2}\right) - 1 - p^2 \leq 0. \tag{6}$$

In this expression, Σ_{eq} is the equivalent Von Mises stress ($=\left(\frac{3}{2}s_{ij}s_{ij}\right)^{\frac{1}{2}}$, $\mathbf{s}$ denoting the deviator of the stress), Σ_m the mean stress ($=\frac{1}{3}\mathrm{tr}\,\boldsymbol{\Sigma}$), Σ_1 and Σ_2 homogeneous quantities with constraints given in the expression will be specified later, p a parameter linked to the porosity f by the formula

$$p = \mathrm{q}f^*, \quad f^* = \begin{cases} f & \text{if } f \le f_c \\ f_c + \delta\left(f - f_c\right) & \text{if } f > f_c \end{cases} \tag{7}$$

where q is the Tvergaard parameter, f_c is the critical porosity at the beginning of coalescence and δ the accelerating factor of cavity growth.

The flow rule associated by normality with this criterion is written:

$$\mathbf{d}^{\mathrm{p}} = \eta\frac{\partial\boldsymbol{\Phi}}{\partial\boldsymbol{\Sigma}} \tag{8}$$

where η denotes the plastic multiplier; by introducing the equivalent plastic strain rate:

$$\mathrm{d}_{eq} = \left(\frac{2}{3}\delta^{\mathrm{p}}_{ij}\,\delta^{\mathrm{p}}_{ij}\right)^{\frac{1}{2}} \tag{9}$$

where $\boldsymbol{\delta}^{\mathrm{p}}$ denotes the deviator of $\mathbf{d}^{\mathrm{p}}$, we can write this flow rule in the form of the expression:

$$\begin{cases} \boldsymbol{\delta}^{\mathrm{p}} = \dfrac{3}{2}\dfrac{\mathrm{d}_{eq}}{\Sigma_{eq}}\mathbf{s} \\ \mathrm{d}^{\mathrm{p}}_{\mathrm{m}} = \dfrac{p}{2}\dfrac{\Sigma_1^2}{\Sigma_2\Sigma_{eq}}sinh\left(\dfrac{3}{2}\dfrac{\Sigma_{\mathrm{m}}}{\Sigma_2}\right)\mathrm{d}_{eq} \end{cases} \tag{10}$$

where $\mathrm{d}^{\mathrm{p}}_{\mathrm{m}} = \frac{1}{3}\,\mathrm{tr}\,\mathbf{d}^{\mathrm{P}}$ is the average part of the plastic strain rate. The evolution of the porosity is given by the following equation, which results from the approximate incompressibility (i.e., neglecting the elasticity) of the metallic matrix:

$$\dot{f} = 3(1-f)\mathrm{d}^{\mathrm{p}}_{\mathrm{m}} \tag{11}$$

Finally, Σ_1 and Σ_2 are functions of the temperature θ and of two parameters of hardening noted ε_{eq} and ε_m [2] and defined by:

$$\varepsilon_{eq} = \int_0^\tau \mathrm{d}_{eq}\,\mathrm{d}\tau, \quad \varepsilon_{\mathrm{m}} = \int_0^\tau \left|\mathrm{d}^{\mathrm{p}}_{\mathrm{m}}\right|\,\mathrm{d}\tau. \tag{12}$$

Let us now consider the case of a kinematic hardening. The expression of the criterion of plasticity is:

$$\frac{\Sigma_{eq}^2}{\Sigma_0^2} + 2p\,sinh\left(\frac{3}{2}\frac{\Sigma_{\mathrm{m}} - \alpha_{\mathrm{m}}}{\Sigma_0}\right) - 1 - p^2 \le 0 \tag{13}$$

where Σ_0 is the elastic limit (depending only on temperature) of the matrix, $\alpha_m = \frac{1}{3}\,\mathrm{tr}\,\alpha$ the mean part of the center α of the domain of elasticity and Σ_{eq} the equivalent von Mises stress defined here by

$$\Sigma_{eq} = \left[\frac{3}{2}\left(s_{ij} - a_{ij}\right)\left(s_{ij} - a_{ij}\right)\right]^{\frac{1}{2}}, \tag{14}$$

$\mathbf{a}$ denoting the deviator of $\boldsymbol{\alpha}$. The expression of p is the same Eq. (7) as for an isotropic hardening. The associated flow rule takes the form:

$$\begin{cases} \boldsymbol{\delta}^{\mathrm{p}} = \dfrac{3}{2}\dfrac{\mathrm{d}_{eq}}{\Sigma_{eq}}(\mathbf{s} - \mathbf{a}) \\ \mathrm{d}^{\mathrm{p}}_{\mathrm{m}} = \dfrac{p}{2}\dfrac{\Sigma_0}{\Sigma_{eq}}sinh\left(\dfrac{3}{2}\dfrac{\Sigma_{\mathrm{m}} - \alpha_{\mathrm{m}}}{\Sigma_0}\right)\mathrm{d}_{eq} \end{cases} \tag{15}$$

where $\delta^{\mathrm{p}}, \mathrm{d}_{eq}$ and $\mathrm{d}^{\mathrm{p}}_{\mathrm{m}}$ are defined as before. The porosity evolution Eq. (11) is unchanged. Finally, the evolution of the center $\mathbf{a}$ of the domain of elasticity is given by:

[2] The rather complicated expressions of Σ_1 and Σ_2 as a function of ε_{eq} and ε_{m} are given in Perrin [6].

$$\begin{cases} \hat{\mathbf{a}} = \frac{2}{3}\left(\frac{\partial\tilde{\alpha}_{eq}}{\partial\varepsilon_{eq}}\right)_T \boldsymbol{\delta}^p + \frac{1}{\tilde{\alpha}_{cq}}\left(\frac{\partial\tilde{\alpha}_{eq}}{\partial\theta}\right)\mathbf{a}\dot{\theta} \\ \dot{\alpha}_m = \left(\frac{\partial\tilde{\alpha}_m}{\partial\varepsilon_m}\right)_T \mathrm{d}_m^p + \frac{1}{\tilde{\alpha}_m}\left(\frac{\partial\tilde{\alpha}_m}{\partial\theta}\right)\alpha_m\dot{\theta} \end{cases} \tag{16}$$

where $\hat{}$ denotes the same objective derivative as in Eq. (2) and Eq. (4) and where $\tilde{\alpha}_{eq}$ and $\tilde{\alpha}_m$ are functions[3] of the same hardening parameters $\varepsilon_{eq}, \varepsilon_m$ as previously. The partial derivatives $\left(\partial\tilde{\alpha}_{eq}\Big/\partial\varepsilon_{eq}\right)$ and $\left(\partial\tilde{\alpha}_m\Big/\partial\varepsilon_m\right)$ are here taken at "triaxiality in deformation" $T = \varepsilon_m\Big/\varepsilon_{eq}$ constant. The terms proportional to $\dot{\theta}$ ensure the cancellation of $\mathbf{a}$ and α_m, therefore of $\boldsymbol{\Sigma}$, at high temperatures. Let us consider finally the case of a mixed isotropic/kinematic hardening ρ indicating the proportion of kinematic hardening. The criterion is written:

$$\frac{\Sigma_{eq}^2}{\left[\rho\Sigma_0 + (1-\rho)\Sigma_1\right]^2} + 2p\ sinh\left(\frac{3}{2}\frac{\Sigma_m - \rho\alpha_m}{\rho\Sigma_0 + (1-\rho)\Sigma_2}\right) - 1 - p^2 \le 0 \tag{17}$$

where

$$\Sigma_{eq} = \left[\frac{3}{2}\left(s_{ij} - \rho a_{ij}\right)\left(s_{ij} - \rho a_{ij}\right)\right]^{\frac{1}{2}}, \tag{18}$$

and the flow rule

$$\begin{cases} \boldsymbol{\delta}^p = \frac{3}{2}\frac{\mathrm{d}_{eq}}{\Sigma_{eq}}(\mathbf{s} - \rho\mathbf{a}) \\ \mathrm{d}_m^p = \frac{p}{2}\frac{\left[\rho\Sigma_0 + (1-\rho)\Sigma_1\right]^2}{\left[\rho\Sigma_0 + (1-\rho)\Sigma_2\right]\Sigma_{eq}} sinh\left(\frac{3}{2}\frac{\Sigma_m - \rho\alpha_m}{\rho\Sigma_0 + (1-\rho)\Sigma_2}\right)\mathrm{d}_{eq}. \end{cases} \tag{19}$$

The laws of evolution of the porosity and of the hardening parameters are the same as previously.

In fact, the cavities being very generally generated by decohesion of the metal matrix around inclusions, f can not become lower than its initial value f_0 (if f is equal to f_0, the cavity is closed around inclusion and the latter prevents its volume from decreasing further). Consequently, all the previous equations are valid only if $f > f_0$, or else $f = f_0$ and $\dot{f} \ge 0 \Leftrightarrow sh \ge 0$ (sh representing the hyperbolic sine of:

$$\frac{3}{2}\frac{\Sigma_m}{\Sigma_2}, \frac{3}{2}\frac{\Sigma_m - \alpha_m}{\Sigma_0} \text{ or } \frac{3}{2}\frac{\Sigma_m - \rho\alpha_m}{\rho\Sigma_0 + (1-\rho)\Sigma_2} \tag{20}$$

depending on the type of hardening). If $f = f_0$ and $sh < 0$, it is necessary to write that the behavior is that of a Von Mises material, which is in fact equivalent to setting $p = 0$ in the previous equations.

2.3. Cavities' nucleation

We have until now, for simplicity, implicitly ignored the phenomena of nucleation of the cavities. Let us now examine their impact. We distinguish two types of nucleation:

- sudden nucleation, governed by a stress criterion developed at the Ecole des Mines de Paris and whose expression is:

$$\Sigma_I + \alpha\left(\tilde{\Sigma}_{eq} - \Sigma_0\right) \le \Sigma_c \tag{21}$$

where Σ_I denotes the greatest principal stress of the stress tensor $\boldsymbol{\Sigma}$, α a dimensionless parameter, Σ_c a critical stress and $\tilde{\Sigma}_{eq}$ the equivalent stress defined by:

$$\tilde{\Sigma}_{eq} = \left(\frac{3}{2}\, s_{ij}s_{ij}\right)^{\frac{1}{2}} \tag{22}$$

($\tilde{\Sigma}_{eq}$ only coincides with Σ_{eq} in the case of isotropic hardening). As long as the inequality is strict in Eq. (13), the behavior is that of a Von Mises material ($\Leftrightarrow p = 0$); when the equality is achieved, f "jumps" abruptly to the value f_0 (and cannot then fall below this value again).

[3] the expressions of which are given in [6].

- Continuous nucleation. We distinguish in this case two contributions, denoted $\dot{f}_{\mathrm{cl}}$ and $\dot{f}_{\mathrm{gl}}$, in the growth rate f porosity. The first represents the rate of increase da at the growth of the cavities, and is given by formula Eq. (11). The second represents the rate of increase due to continuous germination, and is given by an empirical equation

$$\dot{f}_{\mathrm{g}} = \mathrm{A}\mathrm{d}_{\mathrm{eq}} \tag{23}$$

where A is a model parameter.

2.4. Damage delocalization

For some applications (involving high stress and/or strain gradients), the porosity evolution equation is "delocalized". We then define local rates of increase of porosity by growth and nucleation $\dot{f}_{\mathrm{cl}}$ and $\dot{f}_{\mathrm{gl}}$, given by formulas Eq. (11) and Eq. (23) respectively, and the true (nonlocal) growth rate is then given by the convolution formula:

$$\begin{aligned} f(\mathbf{x}) &= \frac{1}{\mathrm{C}(\mathbf{x})}\int_{\Omega} \dot{f}_1(\mathbf{y})\chi(\mathbf{x}-\mathbf{y})\mathrm{d}\Omega_y\ , \\ \dot{f}_1(\mathbf{y}) &\equiv \dot{f}_{\mathrm{cl}}(\mathbf{y}) + \dot{f}_{\mathrm{gl}}(\mathbf{y})\ , \\ C(\mathbf{x}) &= \int_{\Omega} \chi(\mathbf{x}-\mathbf{y})\mathrm{d}\Omega_{\mathbf{y}}\ . \end{aligned} \tag{24}$$

Ω denotes here the studied domain and χ a weighting function, which we take Gaussian in practice:

$$\chi(\mathbf{z}) = exp\left(\frac{-|\mathbf{z}|^2}{l^2}\right), \tag{25}$$

l being a characteristic length (of the order of the spacing between cavities), which plays the same role as the minimum mesh size in the Rousselier model. Note that Enakoutsa et al. ([8], [9], [10], [21], [22], [23], [24], [25], and [26]) conducted comprehensive investigations into damage delocalization, nonlocality, and other advanced techniques within generalized continuum mechanics.

3. Numerical implementation

This section aims to present the digital implementation of the constitutive equations of the nonlocal Gurson model [1], as defined by Leblond et al. [12], for its integration into the finite element calculation code. The essential element of this numerical implementation is the necessary "projection" operation onto the criterion. After specifying the time discretization of the problem, which establishes the notations used, and briefly recalling the two main steps (local and global) associated with the iterative solution of the problem, we describe the algorithm used for this projection.

3.1. Time discretization

The constitutive equations of the models presented above are described by integro-differential relationships in time. Since direct integration of the continuous problem in time is very difficult, we adopt a step-by-step resolution method: we seek to determine the various mechanical parameters at time $t + \Delta t$ given these quantities at time t. Dealing with ductile materials (which exhibit dissipative behavior), we adopt an implicit Euler scheme for most variables. Different perspectives could be considered, but it is not customary because this scheme has become traditional for integrating the behavior relationships of dissipative materials. It is unconditionally stable and allows for exact verification of the coherence condition when the behavior is independent of time.

3.2. Overview of the problem-solving approach

In general, solving a quasi-static evolution problem requires the coupled treatment of two sub-problems: ensuring structural equilibrium and incorporating behavior relations. The approach adopted in our finite calculations code favors displacements as unknowns (rather than internal variables). Roughly speaking, after time discretization, we are led to solve the following system: The equilibrium is expressed in terms of the principle of virtual powers:

$$\int_{\Omega} \boldsymbol{\Sigma} : \mathbf{d}(\mathrm{v})\, d\Omega = \int_{\Omega} f^d \cdot \mathrm{v}\, d\Omega + \int_{\partial\Omega} \mathrm{T}^d \cdot \mathrm{v}\, d\, S \qquad \forall \mathrm{v} \in V_0^{ad} \tag{26}$$

where V_0^{ad} represents the set of kinematically admissible fields, $\boldsymbol{\Sigma}$ is the unknown stress field, T^d and f^d are the imposed volumetric and surface forces. The integration of the behavior relations provides the stress $\boldsymbol{\Sigma}$ at each point as a function of the displacement increment $\Delta\mathrm{u}$ through a nonlinear relationship. The equilibrium Eq. (26) is then written in the form:

$$\mathrm{R}ez(\Delta\mathrm{u}) = \hat{\mathrm{F}}_i - \hat{\mathrm{F}}_e = 0, \tag{27}$$

in the case of discretization using the finite element method. In Eq. (27), Rez is the vector of nodal residuals expressed as the difference between the internal nodal forces $\hat{F}_i$ and the external nodal forces $\hat{F}_e$. Since the system Eq. (27) is nonlinear, its solution cannot be directly obtained as in elasticity problems. The solution is obtained using an iterative method like Newton's method (or one of its variants), with iterations ending when equilibrium is considered achieved. Each iteration consists of two steps: a global step and a local step.

The **global step** consists of calculating the displacements at the structure's nodes, as well as the total strains and stresses at the Gauss points, assuming the plastic deformation increment $\Delta\boldsymbol{\Sigma}^{\mathrm{p}}$ between times t and $t+\Delta t$ is known at every point. In practice, during the first iteration, this increment is assumed to be zero (purely elastic calculation), and in subsequent iterations, it takes the value found at the end of the previous iteration. This step uses the equilibrium equations, the elastic behavior law, and the boundary conditions, resulting in solving a linear system over the entire structure. However, the plasticity equations are not used during this step.

The approach is analogous to solving a classical elasticity problem using the finite element method, with the difference that the total strain includes an additional contribution from plasticity, which plays the role of "initial deformation" (analogous to thermal deformation, for example).

During the **local step**, the final total deformation (or its increment $\Delta\mathbf{d}$), resulting from the previous global step, is considered as given at each point. Then, the increments of elastic and plastic deformation, $\Delta\mathbf{d}^{\mathrm{e}}$ and $\Delta\mathbf{d}^{\mathrm{p}}$, as well as the stress $\boldsymbol{\Sigma}$, are calculated using the equations of plasticity. In no way, during this step, will equilibrium equations or boundary conditions be used, which excludes solving a linear system over the entire structure. The solution algorithm is performed independently at different points.

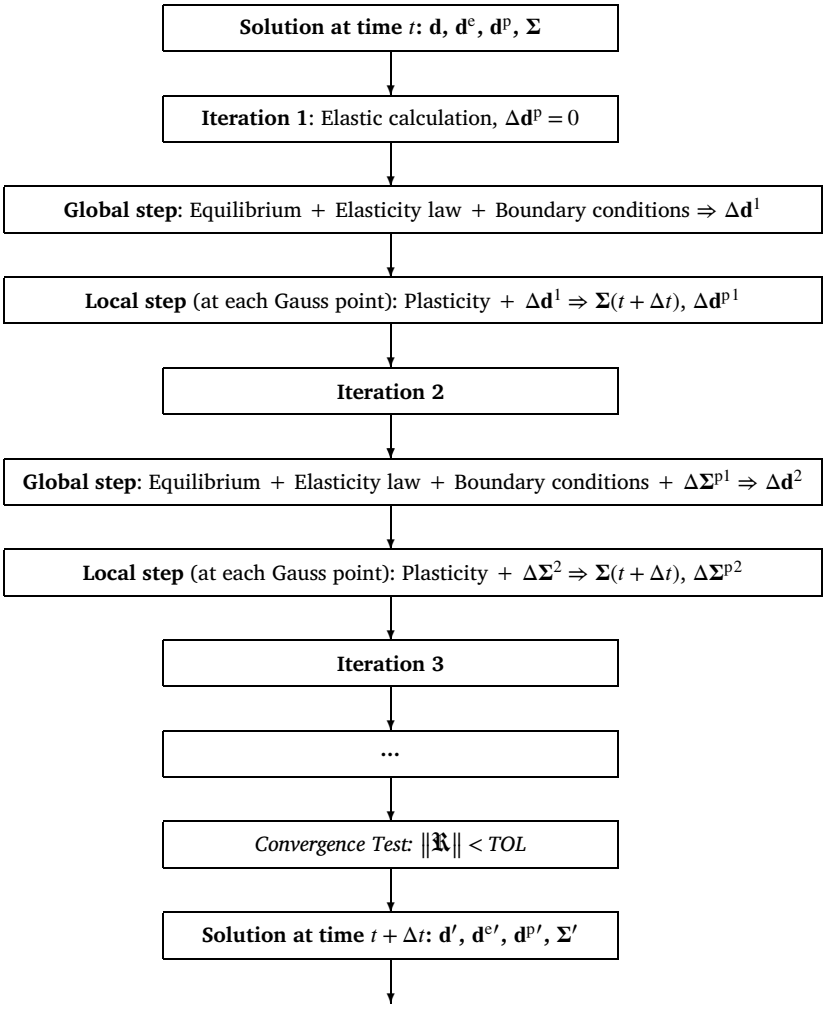

The following diagram summarizes the different steps of the method.

It should be noted that despite the somewhat complex nature that the programming of the global step may take, there is no need to worry about it when digitally implementing a new plasticity model into a finite element calculation code. The only developments

required are related to the local step, which we will now focus on. The reason is quite simple: the model to be implemented is independent of this programming (in fact, it is a general routine that can be used by any other plasticity model). For this reason, we will only focus on the local step in the implementation of the ductile fracture model described above. We will only consider the points in the structure where we are looking for increments in plastic and elastic deformations and stresses. In practice, all Gauss points in the structure are processed successively, but again, there is no need to worry as an automatic procedure, valid for any model that we want to implement, takes care of it and is written once and for all.

Compared to the numerical implementation of the classical elasto-plasticity equations in large transformations, that of the ductile rupture models presents certain differences which mainly concern the so-called operation of "plastic stress correction" (calculation of the stresses and various other mechanical parameters at time $t + \Delta t$, knowing these quantities at time t as well as the increment $\Delta\varepsilon \equiv \mathbf{d}\Delta t$ of total deformation between these two times).

3.3. Implicit algorithm for projecting onto the criterion

3.3.1. Generalities

The numerical implementation of the constitutive equations of the Gurson model, whether in its local or nonlocal version, presents certain differences compared to the digitization of the classical von Mises elasto-plasticity equations. These differences mainly concern the "projection onto the criterion" or "plastic stress correction" operation, which involves calculating stresses and various other mechanical parameters at time $t + \Delta t$, given these quantities at time t as well as the total strain increment $\Delta \mathrm{v} \equiv \varepsilon \Delta t$ between these two instants. (Note that in large transformations, $\varepsilon\Delta t$ is not the variation of the linearized strain tensor, which is not defined. The notation $\Delta\mathbf{v}$ is used to simplify the expressions.)

In everything that follows, we will focus on the incremental problem defined between times t and $t + \Delta t$. Initially, we assume small strains to simplify the presentation. The quantities that appear will be considered at time $t + \Delta t$, unless they are marked with an upper index ^{0}, which indicates that they are considered at time t. The known quantities include $\mathbf{\Sigma}$ (stress), $\bar{\varepsilon}$ (strain), and $\Delta\varepsilon$ (the total strain increment between times t and $t + \Delta t$).

3.3.2. Correction of the stress - case of isotropic hardening

Let us write the discretized equations of the problem, denoting $\Delta\boldsymbol{\varepsilon} \equiv \mathbf{d}\Delta t$, $\Delta\boldsymbol{\varepsilon}^{\mathrm{e}} \equiv \mathbf{d}^{\mathrm{e}}\Delta t, \Delta\boldsymbol{\varepsilon}^{\mathrm{p}} \equiv \mathbf{d}^{\mathrm{p}}\Delta t$, $\Delta\mathbf{e}^{\mathrm{e}}$ and $\Delta\mathbf{e}^{\mathrm{p}}$ the deviatoric parts of $\Delta\boldsymbol{\varepsilon}^{\mathrm{e}}$, and $\Delta\boldsymbol{\varepsilon}^{\mathrm{p}}$, $\Delta\varepsilon^{\mathrm{e}}_{\mathrm{m}}$ and $\Delta\varepsilon^{\mathrm{p}}_{\mathrm{m}}$ their mean parts, assigning a " ′ " the quantities taken at time $t + \Delta t$ (the non-primed quantities are taken at time t), and initially neglecting the effects due temperature variations and major transformations:

- Decomposition of the deformation increment:

$$\Delta\boldsymbol{\varepsilon} = \Delta\boldsymbol{\varepsilon}^{\mathrm{e}} + \Delta\boldsymbol{\varepsilon}^{\mathrm{p}} \tag{28}$$

- Elasticity law:

$$\Delta\mathbf{s} = 2\mu\Delta\mathbf{e}^{\mathrm{e}}, \tag{29}$$

$$\Delta\Sigma_{\mathrm{m}} = (3\lambda + 2\mu)\Delta\varepsilon^{\mathrm{e}}_{\mathrm{m}} \tag{30}$$

- Yield criteria:

$$\frac{\Sigma'^{\,2}_{\mathrm{eq}}}{\Sigma'^{2}_{1}} + 2\tilde{p}'\, cosh\left(\frac{3}{2}\frac{\Sigma'_{\mathrm{m}}}{\Sigma'_{2}}\right) - 1 - \tilde{p}'^{2} = 0 \tag{31}$$

- Plastic flow rule:

$$\Delta\mathbf{e}^{\mathrm{p}} = \frac{3}{2}\frac{\Delta\varepsilon_{\mathrm{eq}}}{\Sigma'_{\mathrm{eq}}}\mathbf{s}', \tag{32}$$

$$\Delta\varepsilon^{\mathrm{p}}_{\mathrm{m}} = \frac{\tilde{p}''}{2}\frac{\Sigma'^{2}_{1}}{\Sigma'_{2}\Sigma'_{\mathrm{eq}}}\, sinh\left(\frac{3}{2}\frac{\Sigma'_{\mathrm{m}}}{\Sigma'_{2}}\right)\Delta\varepsilon_{\mathrm{eq}}. \tag{33}$$

- Definition of Σ'_1 and Σ'_2:

$$\begin{aligned}\Sigma'_1 &\equiv \Sigma_1\left(\varepsilon'_{\mathrm{eq}}, \varepsilon'_{\mathrm{m}}\right),\\ \Sigma'_2 &\equiv \Sigma_2\left(\varepsilon'_{\mathrm{eq}}, \varepsilon'_{\mathrm{m}}\right)\end{aligned} \tag{34}$$

- Evolution equation of the hardening parameters:

$$\begin{aligned}\Delta\varepsilon_{\mathrm{eq}} &= \left(\tfrac{2}{3}\Delta\mathrm{e}^{\mathrm{p}}_{\mathrm{ij}}\Delta\mathrm{e}^{\mathrm{p}}_{\mathrm{ij}}\right)^{\frac{1}{2}}.\\ \Delta\varepsilon_{\mathrm{m}} &= \left|\Delta\varepsilon^{\mathrm{p}}_{\mathrm{m}}\right|.\end{aligned} \tag{35}$$

Only Eq. (31) and Eq. (33) call for specific comments here:

- To be perfectly logical, it would be necessary to use in Eq. (31), which constitutes the writing of the criterion at the instant $t+\Delta t$, the quantity $p' \equiv p(t+\Delta t)$ deriving, via Eq. (7), from the real porosity f' at this instant. This porosity being unknown, the algorithm is then implicit in relation to this variable (as in relation to the others). The numerical experiment however showed that the convergence is very difficult, even impossible, with such an algorithm, and that one can, in practice, obtain results only with an explicit algorithm compared to the porosity (but however implicit against all other parameters). We therefore replace in Eq. (31) the quantity p' by an approximation noted $\tilde{p}'$, deriving via Eq. (7), from the estimation of $\tilde{f}'$ of $f' \equiv f(t+\Delta t)$ given by

$$\tilde{f}' \equiv f(t) + \dot{f}(t)\Delta t. \tag{36}$$

  This of course requires storing the rate of increase $\dot{f}$ of the porosity.
- In equation (33), which gives the increase in average plastic deformation between the times t and $t+\Delta t$, the most precise would be to use the quantity $p'' = p(t+\Delta t/2)$ (deriving from the true porosity (f'' to $t+\Delta t/2$) In order to preserve however the explicit character of the algorithm with respect to porosity, we replace p'' by the approximation $\tilde{p}''$ derived from the approximate porosity

$$\tilde{f}'' \equiv f(t) + f(t)\frac{\Delta t}{2}. \tag{37}$$

The beginning of the resolution of these equations follows the classic approach: we add $\mathbf{s}$ to the two members of Eq. (29) taking into account Eq. (30) and Eq. (31):

$$\mathbf{s}' \equiv \mathbf{s} + \Delta\mathbf{s} = \mathbf{s} + 2\mu\Delta\mathbf{e} - 2\mu\Delta\mathbf{e}^{\mathrm{p}} = \mathbf{s}^* - 3\mu\frac{\Delta\varepsilon_{\mathrm{eq}}}{\Sigma'_{\mathrm{eq}}}\mathbf{s}' \tag{38}$$

where

$$\mathbf{s}^* \equiv \mathbf{s} + 2\mu\Delta\mathbf{e} \quad (\Delta\mathbf{e} \equiv \text{ deviator of } \Delta\boldsymbol{\varepsilon}) \tag{39}$$

is the final stress deviator "computed elastically", i.e. assuming the increment $\Delta\varepsilon$ of purely elastic total deformation (known quantity since we know $\mathbf{s}$ and $\Delta\mathrm{e}$). This implies that, as usual, $\mathbf{s}'$ and $\mathbf{s}^*$ are parallel, so that we can replace $\mathbf{s}' \Big/ \Sigma'_{\mathrm{eq}}$ by $\mathbf{s}^* \Big/ \Sigma^*_{\mathrm{eq}}$ where $\left(\Sigma^*_{\mathrm{eq}} \equiv \left(\frac{3}{2}s^*_{\mathrm{ij}}s^*_{\mathrm{ij}}\right)^{\frac{1}{2}}\right)$ in the flow rule Eq. (33) and the calculation of $\Delta\mathbf{e}^{\mathrm{p}}$ is reduced to that of $\Delta\varepsilon_{\mathrm{eq}}$. Moreover, taking the Von Mises function of the two members, we also deduce that

$$\Sigma^*_{\mathrm{eq}} - \Sigma'_{\mathrm{eq}} = 3\mu\Delta\varepsilon_{\mathrm{eq}} \tag{40}$$

again a classic equation. By adding in the same way Σ_{m} to the two members of Eq. (30) taking into account Eq. (29), we obtain the same

$$\Sigma^*_{\mathrm{m}} - \Sigma'_{\mathrm{m}} = (3\lambda + 2\mu)\Delta\varepsilon^{\mathrm{p}}_{\mathrm{m}}, \tag{41}$$

where

$$\Sigma^*_{\mathrm{m}} \equiv \Sigma_{\mathrm{m}} + (3\lambda + 2\mu)\Delta E_{\mathrm{m}} \tag{42}$$

(ΔE_{m} mean part of $\Delta\varepsilon$[4]) denotes the "elastically calculated" (known) final mean stress. Combining Eq. (29) and Eq. (42), we get:

$$\frac{\Delta\varepsilon^{\mathrm{p}}_{\mathrm{m}}}{\Delta\varepsilon_{\mathrm{eq}}} = \frac{3\mu}{3\lambda+2\mu}\frac{\Sigma^*_{\mathrm{m}} - \Sigma'_{\mathrm{m}}}{\Sigma^*_{\mathrm{eq}} - \Sigma'_{\mathrm{eq}}}. \tag{43}$$

Relating this equation to Eq. (33), we get

$$\frac{3\mu}{3\lambda+2\mu}\frac{\Sigma^*_{\mathrm{m}} - \Sigma'_{\mathrm{m}}}{\Sigma^*_{\mathrm{eq}} - \Sigma'_{\mathrm{eq}}} = \frac{\tilde{p}''}{2}\frac{\Sigma'^2_1}{\Sigma'_2\Sigma'_{\mathrm{eq}}}sinh\left(\frac{3}{2}\frac{\Sigma'_{\mathrm{m}}}{\Sigma'_2}\right). \tag{44}$$

The problem is reduced to the resolution of Eq. (31), Eq. (34), Eq. (35)$_2$, Eq. (40), Eq. (41) and Eq. (44) with respect to the unknowns $\Sigma'_{\mathrm{eq}}, \Sigma'_{\mathrm{m}}, \Sigma'_1, \Sigma'_2, \Delta\varepsilon_{\mathrm{eq}}, \Delta\varepsilon^{\mathrm{p}}_{\mathrm{m}}$ and $\Delta\varepsilon_{\mathrm{m}}$. For this, we adopt an iterative approach with respect to the unknowns $\Delta\varepsilon_{\mathrm{eq}}, \Delta\varepsilon^{\mathrm{p}}_{\mathrm{m}}, \Delta\varepsilon_{\mathrm{m}}, \Sigma'_1, \Sigma'_2$: starting from certain initial values of these parameters, we solve (we will see how) Eq. (31) and Eq. (44) by compared to Σ'_{eq} and Σ'_{m}, we deduce $\Delta\varepsilon_{\mathrm{eq}}, \Delta\varepsilon^{\mathrm{p}}_{\mathrm{m}}$ and $\Delta\varepsilon_{\mathrm{m}}$ with Eq. (40), Eq. (41) and Eq. (35)$_2$, then Σ'_1 and Σ'_2 by Eq. (34) and we iterate the process until convergence.

[4] The notation E_{m} is used here to avoid confusion with the hardening parameter ε_{m}.

The whole problem therefore consists of simultaneously solving Eq. (31) and Eq. (44) with respect to Σ'_{eq} and Σ'_{m}, the other parameters being assumed to be known. For this, we use the following parametrization (inspired by that of an ellipse) of the flow surface Eq. (31):

$$\begin{cases} \Sigma'_{eq} = \left(1-\tilde{p}'\right)\Sigma'_1 cos\varphi \\ \\ \Sigma'_{m} = \dfrac{2}{3}\Sigma'_2 sgn(\varphi) arsinh\left[1+\dfrac{\left(1-\tilde{p}'\right)^2}{2p'}sin^2\varphi\right]. \end{cases} \quad \left(-\frac{\pi}{2}\le\varphi\le\frac{\pi}{2}\right). \tag{45}$$

The problem is then to solve the following equation, taken from Eq. (44), with respect to the unique variable φ:

$$\mathcal{F}(\varphi) = \mathrm{a}\left[\Sigma^*_m - \Sigma'_m(\varphi)\right] cos\varphi\, \tilde{p}''\left[\Sigma^*_{eq} - \Sigma'_{eq}(\varphi)\right] sinh\left[\frac{3}{2}\frac{\Sigma'_m(\varphi)]}{\Sigma'_2}\right] = 0 \tag{46}$$

where

$$\mathrm{a} \equiv 2\left(1-\tilde{p}'\right)\frac{\Sigma'_2}{\Sigma'_1}\frac{3\mu}{3\lambda+2\mu} \tag{47}$$

It is sufficient for that to use the method of Newton; one easily calculates for this purpose:

$$\begin{aligned} \mathcal{F}(\varphi) = -\, sin\varphi\Bigg(&\mathrm{a}\left[\Sigma^*_m - \Sigma'_m(\varphi) + \frac{2\left(1-\tilde{p}'\right)^2\Sigma'_2\cos^2\varphi}{3\tilde{p}' sinh\left(\dfrac{3}{2}\dfrac{\Sigma'_m(\varphi)}{\Sigma'_2}\right)}\right] \\ &+ \tilde{p}''\left(1-\tilde{p}'\right)\Sigma'_1 sinh\left(\frac{3}{2}\frac{\Sigma'_m(\varphi)}{\Sigma'_2}\right) \\ &+ \frac{\tilde{p}''}{\tilde{p}'}\left(1-\tilde{p}'\right)^2\left[\Sigma^*_{eq} - \Sigma'_{eq}(\varphi)\right] cos\varphi\, coth\left(\frac{3}{2}\frac{\Sigma'_m(\varphi)}{\Sigma'_2}\right)\Bigg). \end{aligned} \tag{48}$$

Most of the numerical solution therefore consists of two nested loops, the outer loop carrying out the iterations on the parameters $\Sigma'_1, \Sigma'_2, \Delta\epsilon_{eq}, \Delta\epsilon^{p}_{m}$ and $\Delta\epsilon_m$, the inner loop solving Eq. (46) by Newton's method. Once this calculation is complete, the program evaluates the local porosity increment Δf_1 using the following discretized version of Eq. (11) and Eq. (23):

$$\Delta f_1 = \Delta f_{cl} + \Delta f_{gl},\ \Delta f_{cl} = 3\left(1-\tilde{f}'\right)\Delta\epsilon^{p}_{m},\ \Delta f_{gl} = \mathrm{A}\epsilon_{eq}.$$

Let us now indicate the modifications made by taking into account temperature variations and major transformations. It is then necessary to add the increment of thermal deformation $\Delta\epsilon^{t}$ in the second member of Eq. (28). In addition, Eq. (29) and Eq. (30) should be replaced by:

$$\begin{cases} \Delta\mathbf{s} + (\Delta\mathbf{s})_{J\text{ or }M} \equiv 2\mu'\Delta\mathbf{e}^{e} + \dfrac{\Delta E}{E}\mathbf{s},\ (\Delta\mathbf{s})_{J\text{ or }M} \equiv \Sigma\cdot\Delta\boldsymbol{\Omega} - \Delta\boldsymbol{\Omega}\cdot\Sigma \\ \\ \Delta\Sigma_m = \left(3\lambda'+2\mu'\right)\Delta\epsilon^{e}_{m} + \dfrac{\Delta E}{E}\Sigma_m \end{cases} \tag{49}$$

where $\Delta\boldsymbol{\Omega} = \boldsymbol{\Omega}\Delta t$ represents the rotation increment.[5] In these equations, the Lamé coefficients λ' and μ' are taken at time $t+\Delta t$, but the Young's modulus E and the stresses $\boldsymbol{\Sigma}, \mathbf{s}, \Sigma_m$ at the time t.

The approach is then the same as before, but adding $\mathbf{s} - (\Delta\mathbf{s})_{J\text{ or }M}$ to the two members of Eq. $(49)_1$ instead of $\mathbf{s}$; the equations obtained are the same as before provided that expressions Eq. (39) and Eq. (41) of $\mathbf{s}^*$ and Σ^*_m are modified as follows:

$$\begin{cases} \mathbf{s}^* = \mathbf{s} + 2\mu'\Delta\mathbf{e}^{e} - (\Delta\mathbf{s})_{J\text{ or }M} + \dfrac{\Delta E}{E}\mathbf{s}, \\ \\ \Sigma^*_m = \Sigma_m + \left(3\lambda'+2\mu'\right)\left(\Delta E_m - \Delta\epsilon^{t}_{m}\right) + \dfrac{\Delta E}{E}\Sigma_m. \end{cases} \tag{50}$$

The rest of the resolution is unchanged except for these changes (and the $\lambda\to\lambda'$ and $\mu\to\mu'$ substitutions.) In practice, the corrective terms $-(\Delta\mathbf{s})_{J\text{ or }M}$, $\dfrac{\Delta E}{E}\mathbf{s}$, $-\left(3\lambda'+2\mu'\right)\Delta\epsilon^{t}$ and $\dfrac{\Delta E}{E}\Sigma_m$ are added to $\mathbf{s}^*$ and Σ^*_m.

[5] Note that the expression of $\Delta\Sigma_m$ does not include a corrective term to the objective derivative; this is because the trace $\boldsymbol{\Sigma}\cdot\boldsymbol{\Omega} - \boldsymbol{\Omega}\cdot\boldsymbol{\Sigma}$ is zero (consequence of $\mathrm{tr}(\mathbf{A}\cdot\mathbf{B}) = \mathrm{tr}(\mathbf{B}\cdot\mathbf{A})$).

3.3.3. Stress correction - case of kinematics hardening

The discretized equations of the problem are written here, with notations analogous to those of the isotropic case:

$$\begin{cases} \Delta\boldsymbol{\varepsilon} = \Delta\boldsymbol{\varepsilon}^{\mathrm{e}} + \Delta\boldsymbol{\varepsilon}^{p} + \boldsymbol{\varepsilon}^{\mathrm{t}} \\ \Delta\mathbf{s} + (\Delta\mathbf{s})_{\mathrm{J\ or\ M}} = 2\mu\Delta\mathbf{e}^{\mathrm{e}} + \dfrac{\Delta \mathrm{E}}{\mathrm{E}}\mathbf{s}, \\ \Delta\Sigma_{\mathrm{m}} = (3\lambda + 2\mu)\,\Delta\varepsilon_{\mathrm{m}}^{\mathrm{e}} + \dfrac{\Delta \mathrm{E}}{\mathrm{E}}\Sigma_{\mathrm{m}} \end{cases}$$

$$\begin{cases} \dfrac{\Sigma_{\mathrm{eq}}'^2}{\Sigma_0'^2} + 2\tilde{p}' cosh\left(\dfrac{3}{2}\dfrac{\Sigma_{\mathrm{m}}' - \alpha_{\mathrm{m}}'}{\Sigma_0'}\right) - 1 - \tilde{p}'^2 = 0 \\ \Sigma_{\mathrm{eq}}' = \left[\dfrac{3}{2}\left(s_{ij}' - \mathrm{a}_{ij}'\right)\left(\mathrm{s}_{ij}' - \mathrm{a}_{ij}'\right)\right]^{\frac{1}{2}} \end{cases}$$

$$\begin{cases} \Delta\mathbf{e}^{\mathrm{p}} = \dfrac{3}{2}\dfrac{\Delta\varepsilon_{\mathrm{eq}}}{\Sigma_{\mathrm{eq}}'}\left(\mathbf{s}' - \mathbf{a}'\right), \\ \Delta\varepsilon_{\mathrm{m}}^{\mathrm{p}} = \dfrac{\tilde{p}''}{2}\dfrac{\Sigma_0'}{\Sigma_{\mathrm{eq}}'} sinh\left(\dfrac{3}{2}\dfrac{\Sigma_{\mathrm{m}}' - \alpha_{\mathrm{m}}'}{\Sigma_0'}\right)\Delta\varepsilon_{\mathrm{eq}}. \end{cases} \tag{51}$$

$$\begin{cases} \Delta\mathbf{a} + (\Delta\mathbf{a})_{\mathrm{J\,or\,M}} = \dfrac{2}{3}\left(\dfrac{\Delta\tilde{\alpha}_{\mathrm{eq}}}{\Delta\varepsilon_{\mathrm{eq}}}\right)_T \Delta\mathbf{e}^{\mathrm{P}} + \dfrac{1}{\tilde{\alpha}_{\mathrm{eq}}}\left(\dfrac{\Delta\tilde{\alpha}_{\mathrm{eq}}}{\Delta\theta}\right)\mathbf{a}\Delta\theta, \\ (\Delta\mathbf{a})_{\mathrm{J\,or\,M}} = \mathbf{a}\cdot\Delta\Omega - \Delta\Omega\cdot\mathbf{a} \\ \Delta\alpha_{\mathrm{m}} = \left(\dfrac{\Delta\tilde{\alpha}_{\mathrm{m}}}{\Delta\varepsilon_{\mathrm{m}}}\right)_T \Delta\varepsilon_{\mathrm{m}}^{\mathrm{p}} + \dfrac{1}{\tilde{\alpha}_{\mathrm{m}}}\left(\dfrac{\Delta\tilde{\alpha}_{\mathrm{m}}}{\Delta\theta}\right)\alpha_{\mathrm{m}}\Delta\theta \end{cases}$$

$$\begin{cases} \tilde{\alpha}_{\mathrm{eq}} \equiv \tilde{\alpha}_{\mathrm{eq}}\left(\varepsilon_{\mathrm{eq}}, \varepsilon_{\mathrm{m}}, \theta\right), \quad \tilde{\alpha}_{\mathrm{m}} \equiv \tilde{\alpha}_{\mathrm{m}}\left(\varepsilon_{\mathrm{eq}}, \varepsilon_{\mathrm{m}}, \theta\right) \\ \Delta\varepsilon_{\mathrm{eq}} = \left(\dfrac{2}{3}\Delta\mathrm{e}_{ij}^{\mathrm{p}}\cdot\Delta\mathrm{e}_{ij}^{\mathrm{p}}\right)^{\frac{1}{2}}, \Delta\varepsilon_{\mathrm{m}} = \left|\Delta\varepsilon_{\mathrm{m}}^{\mathrm{p}}\right| \end{cases}$$

As usual, the secants $\left(\Delta\tilde{\alpha}_{\mathrm{eq}}\Big/\Delta\varepsilon_{\mathrm{eq}}\right)_T$ and $\left(\Delta\tilde{\alpha}_{\mathrm{m}}\Big/\Delta\varepsilon_{\mathrm{m}}\right)_T$ are taken at the final temperature θ', and the secants $\left(\Delta\tilde{\alpha}_{\mathrm{eq}}\Big/\Delta\theta\right)$ and $\left(\Delta\tilde{\alpha}_{\mathrm{m}}\Big/\Delta\theta\right)$ has the initial $\left(\varepsilon_{\mathrm{eq}}, \varepsilon_{\mathrm{m}}\right)$ deformation. Moreover, the first two secants are taken at constant triaxiality equal to the initial triaxiality $T = \varepsilon_{\mathrm{m}}/\varepsilon_{\mathrm{eq}}$.

Adding $\mathbf{s} - (\Delta\mathbf{s})_{\mathrm{J\ or\ M}} - \mathbf{a} - \Delta\mathbf{a}$ to both members from Eq. $(51)_{2,3}$ we get

$$\mathbf{s}' - \mathbf{a}' \equiv \mathbf{s} + \Delta\mathbf{s} - \mathbf{a} - \Delta\mathbf{a} = \mathbf{s} + 2\mu'\Delta\mathbf{e}^{\mathrm{e}} - (\Delta\mathbf{s})_{\mathrm{J\ or\ M}} + \frac{\Delta \mathrm{E}}{\mathrm{E}}\mathbf{s} - \mathbf{a} - \Delta\mathbf{a}$$

which yields, taking into account Eq. $(51)_1$, Eq. $(51)_7$, Eq. $(51)_9$:

$$\mathbf{s}' - \mathbf{a}' = \mathbf{s} + 2\mu'\Delta\mathbf{e} - (\Delta\mathbf{s})_{\mathrm{J\ or\ M}} + \frac{\Delta \mathrm{E}}{\mathrm{E}}\mathbf{s} - \mathbf{a} - \frac{2}{3}\left(\frac{\Delta\tilde{\alpha}_{\mathrm{eq}}}{\Delta\varepsilon_{\mathrm{eq}}}\right)_T \frac{3}{2}\frac{\Delta\varepsilon_{\mathrm{eq}}}{\Sigma_{\mathrm{eq}}'}\left(\mathbf{s}' - \mathbf{a}'\right) \tag{52}$$

$$+ (\Delta\mathbf{a})_{\mathrm{J\ or\ M}} - \frac{1}{\tilde{\alpha}_{\mathrm{eq}}}\left(\frac{\Delta\tilde{\alpha}_{\mathrm{eq}}}{\Delta\theta}\right)\mathbf{a}\Delta\theta - 2\mu'\frac{3}{2}\frac{\Delta\varepsilon_{\mathrm{eq}}}{\Sigma_{\mathrm{eq}}'}\left(\mathbf{s}' - \mathbf{a}'\right).$$

Assuming

$$\mathbf{s}^{*} = \mathbf{s} + 2\mu'\Delta\mathbf{e} - (\Delta\mathbf{s})_{\mathrm{J\ or\ M}} + \frac{\Delta \mathrm{E}}{\mathrm{E}}\mathbf{s} - \mathbf{a} + (\Delta\mathbf{a})_{\mathrm{J\ or\ M}} - \frac{1}{\tilde{\alpha}_{\mathrm{eq}}}\left(\frac{\Delta\tilde{\alpha}_{\mathrm{eq}}}{\Delta\theta}\right)\mathbf{a}\Delta\theta \tag{53}$$

($\mathbf{s}^{*}$ is a known quantity), this is written

$$\mathbf{s}' - \mathbf{a}' = \mathbf{s}^* - \left[3\mu' + \left(\frac{\Delta\tilde{\alpha}_{eq}}{\Delta\varepsilon_{eq}}\right)_T\right]\frac{\Delta\varepsilon_{eq}}{\Sigma'_{eq}}\left(\mathbf{s}' - \mathbf{a}'\right) \tag{54}$$

equation which shows that $\mathbf{s}' - \mathbf{a}'$ and $\mathbf{s}^*$ are parallel and reduces, as in the isotropic case, the computation from Δe^p to that of $\Delta\varepsilon_{eq}$. Moreover, taking the Von Mises function of the two members, we obtain by setting

$$\Sigma^*_{eq} = \left(\frac{3}{2}s^*_{ij}s^*_{ij}\right)^{\frac{1}{2}}, \tag{55}$$

the equation

$$\Sigma^*_{eq} - \Sigma'_{eq} = \left[3\mu' + \left(\frac{\Delta\tilde{\alpha}_{eq}}{\Delta\varepsilon_{eq}}\right)_T\right]\Delta\varepsilon_{eq}, \tag{56}$$

analogous to Eq. (40) of the isotropic case.

Similarly, adding $\Sigma_m - \alpha_m - \Delta\alpha_m$ to both sides of Eq. $(51)_3$, we obtain:

$$\Sigma'_m - \alpha'_m \equiv \Sigma_m + \Delta\Sigma_m - \alpha_m - \Delta\alpha_m = \Sigma_m + \left(3\lambda' + 2\mu'\right)\Delta\varepsilon^e_m + \frac{\Delta E}{E}\Sigma_m - \alpha_m - \Delta\alpha_m, \tag{57}$$

which yields, taking into account Eq. $(51)_1$ and $(51)_8$:

$$\Sigma^*_m - \left(\Sigma'_m - \alpha'_m\right) = \left[3\lambda' + 2\mu' + \left(\frac{\Delta\tilde{\alpha}_m}{\Delta\varepsilon_m}\right)_T\right]\Delta\varepsilon^p_m, \tag{58}$$

where Σ^*_m denotes the (known) quantity defined by:

$$\Sigma^*_m = \Sigma_m + \left(3\lambda' + 2\mu'\right)\left(\Delta E_m - \Delta\varepsilon^t_m\right) + \frac{\Delta E}{E}\Sigma_m - \alpha_m - \frac{1}{\tilde{\alpha}_m}\left(\frac{\Delta\tilde{\alpha}_m}{\Delta\theta}\right)\alpha_m\Delta\theta; \tag{59}$$

Eq. (58) is analogous to Eq. (41) in the isotropic case. Now combining Eq. $(51)_5$, Eq. (56) and Eq. (58), we get:

$$\frac{3\mu' + \left(\frac{\Delta\tilde{\alpha}_{eq}}{\Delta\varepsilon_{eq}}\right)_T}{3\lambda' + 2\mu' + \left(\frac{\Delta\tilde{\alpha}_m}{\Delta\varepsilon_m}\right)_T}\frac{\Sigma^*_m - \left(\Sigma'_m - \alpha'_m\right)}{\Sigma^*_{eq} - \Sigma'_{eq}} = \frac{\tilde{p}''}{2}\frac{\Sigma'_0}{\Sigma'_{eq}}sinh\left(\frac{3}{2}\frac{\Sigma'_m - \alpha'_m}{\Sigma'_0}\right), \tag{60}$$

equation analogous to Eq. (44).

From there, we adopt an iterative resolution method, as in the case of isotropic work hardening starting from initial values of the parameters:

$$\Delta\varepsilon_{eq},\ \Delta\varepsilon^p_m,\ \Delta\varepsilon_m,\ \left(\frac{\Delta\tilde{\alpha}_{eq}}{\Delta\varepsilon_{eq}}\right)_T,\ \left(\frac{\Delta\tilde{\alpha}_m}{\Delta\varepsilon_m}\right)_T, \tag{61}$$

we start by solving the Eq. $(51)_2$ and Eq. (60) with respect to Σ_{eq} and $\Sigma'_m - \alpha'_m$; as these equations are identical to those Eq. (31) and Eq. (44) of the isotropic case on condition of replacing $\Sigma'_1, \Sigma'_2, 3\mu, 3\lambda + 2\mu, \Sigma'_m$ with

$$\Sigma'_0, \Sigma'_0, 3\mu' + \left(\frac{\Delta\tilde{\alpha}_{eq}}{\Delta\varepsilon_{eq}}\right)_T, 3\lambda + 2\mu + \left(\frac{\Delta\vec{\alpha}_m}{\Delta\varepsilon_m}\right)_T, \Sigma'_m - \alpha'_m, \tag{62}$$

it suffices to employ the same method with these substitutors; then we draw $\Delta\varepsilon_{eq}, \Delta\varepsilon^p_m$ and $\Delta\varepsilon_m$ from Eq. (56), Eq. (58), Eq. $(35)_2$, we deduce

$$\left(\frac{\Delta\tilde{\alpha}_{eq}}{\Delta\varepsilon_{eq}}\right)_T \text{ and } \left(\frac{\Delta\tilde{\alpha}_m}{\Delta\varepsilon_m}\right)_T \tag{63}$$

thanks to Eq. $(51)_{11}$ and we iterate the process until convergence.

When this calculation is finished, it is not only necessary to calculate, as in the isotropic case, the local increment of porosity Δf_1, but also to evolve $\mathbf{a}$ and α_m according to formula Eq. $(51)_{6,7,8}$.

3.3.4. *Stress correction - case of mixed isotropic / kinematic hardening*

The discretized equations of the problem are the same as in the kinematic case, with the exception of Eq. $(51)_{2,3}$ and Eq. $(51)_{4,5}$ which are written here:

$$\begin{cases} \dfrac{\Sigma'^2_{eq}}{\left[\rho\Sigma'_0+(1-\rho)\Sigma'_1\right]^2}+2\tilde{p}'cosh\left(\dfrac{3}{2}\dfrac{\Sigma'_m-\rho\alpha'_m}{\rho\left(\Sigma'_0+(1-\rho)\Sigma'_2\right)}\right)-1-\tilde{p}^2=0, \\ \Sigma'_{eq}\equiv\left[\dfrac{3}{2}\left(s'_{ij}-\rho a'_{ij}\right)\left(s'_{ij}-\rho a'_{ij}\right)\right]^{\frac{1}{2}}. \end{cases} \tag{64}$$

$$\begin{cases} \Delta\mathbf{e}^p=\dfrac{3}{2}\dfrac{\Delta\varepsilon_{eq}}{\Sigma'_{eq}}\left(\mathbf{s}'-\rho\mathbf{a}'\right), \\ \Delta\varepsilon^p_m=\dfrac{\tilde{p}''}{2}\dfrac{\left[\rho\Sigma'_0+(1-\rho)\Sigma'_1\right]^2}{\left[\rho\Sigma'_0+(1-\rho)\Sigma'_2\right]\Sigma'_{eq}}sinh\left(\dfrac{3}{2}\dfrac{\Sigma'_m-\rho\alpha'_m}{\left[\rho\Sigma'_0+(1-\rho)\Sigma'_2\right]}\right)\Delta\varepsilon_{eq} \end{cases} \tag{65}$$

In these equations, Σ'_1 and Σ'_2 are given by:
$\Sigma'_1\equiv\Sigma_1(\varepsilon'_{eq},\varepsilon'_m,\theta')$, $\Sigma'_2\equiv\Sigma_2(\varepsilon'_{eq},\varepsilon'_m,\theta')$.

We do not repeat here the whole approach and we will content ourselves with indicating how the final equations must be modified with respect to the kinematic case: Eq. (53) and Eq. (59) become

$$\mathbf{s}^*=\mathbf{s}+2\mu'\Delta\mathbf{e}-(\Delta\mathbf{s})_{J\text{ or }M}+\frac{\Delta E}{E}\mathbf{s}-\rho\mathbf{a}+\rho(\Delta a)_{J\text{ or }M}-\frac{1}{\tilde{\alpha}_{eq}}\left(\frac{\Delta\tilde{\alpha}_{eq}}{\Delta\theta}\right)\rho\mathbf{a}\Delta\theta \tag{66}$$

$$\Sigma^*_{eq}-\Sigma'_{eq}=\left[3\mu'+\rho\left(\frac{\Delta\tilde{\alpha}_{eq}}{\Delta\varepsilon_{eq}}\right)_T\right]\Delta\varepsilon_{eq} \tag{67}$$

and the Eq. (58) and Eq. (54)

$$\Sigma^*_m-\left(\Sigma'_m-\rho\alpha'_m\right)=\left[3\lambda'+2\mu'+\rho\left(\frac{\Delta\tilde{\alpha}_m}{\Delta\varepsilon_m}\right)_T\right]\Delta\varepsilon^p_m \tag{68}$$

$$\Sigma^*_m=\Sigma_m+\left(3\lambda'+2\mu'\right)\left(\Delta E_m-\Delta\varepsilon^t_m\right)+\frac{\Delta E}{E}\Sigma_m-\rho\alpha_m-\frac{1}{\tilde{\alpha}_m}\left(\frac{\Delta\tilde{\alpha}_m}{\Delta\varepsilon_m}\right)\rho\alpha_m\Delta\theta, \tag{69}$$

and the Eq. (60).

$$\frac{3\mu'+\rho\left(\dfrac{\Delta\tilde{\alpha}_{eq}}{\Delta\varepsilon_{eq}}\right)_T}{3\lambda'+2\mu'+\rho\left(\dfrac{\Delta\tilde{\alpha}_m}{\Delta\varepsilon_m}\right)_T}\frac{\Sigma^*_m-\left(\Sigma'_m-\rho\alpha'_m\right)}{\Sigma^*_{eq}-\Sigma'_{eq}}=\frac{\tilde{p}''}{2}\frac{\left[\rho\Sigma'_0+(1-\rho)\Sigma'_1\right]^2}{\left[\rho\Sigma'_0+(1-\rho)\Sigma'_2\right]\Sigma'_{eq}}sinh\left(\frac{3}{2}\frac{\Sigma'_m-\rho\alpha'_m}{\rho\Sigma'_0+(1-\rho)\Sigma'_2}\right) \tag{70}$$

The system of the two Eq. $(51)_{2,3}$ and Eq. (60) is solved with respect to the unknowns Σ'_{eq} and $\Sigma'_m-\rho\alpha'_m$ by the same method as in the isotropic case (Eq. (45), Eq. (46), Eq. (47), Eq. (48)), with the substitutions

- $\Sigma'_1\to\rho\Sigma'_0+(1-\rho)\Sigma'_1$
- $\Sigma'_2\to\rho\Sigma'_0+(1-\rho)\Sigma'_2$,
- $3\mu\to3\mu'+\rho\left(\Delta\tilde{\alpha}_{eq}/\Delta\varepsilon_{eq}\right)_T$,
- $3\lambda+2\mu\to3\lambda'+2\mu'+\rho\left(\Delta\tilde{\alpha}_m/\Delta\varepsilon_m\right)_T$,
- $\Sigma'_m\to\Sigma'_m-\rho\alpha'_m$.

The rest of the resolution is the same as in the kinematic case. Note that in practice, the substitutions:

- $\Sigma'_1\to\rho\Sigma'_0+(1-\rho)\Sigma'_1$,
- $\Sigma'_2\to\rho\Sigma'_0+(1-\rho)\Sigma'_2$,
- $\tilde{\alpha}_{eq}\to\rho\tilde{\alpha}_{eq}$:
- $\tilde{\alpha}_m\to\rho\tilde{\alpha}_m$.

3.4. Particular cases

The first particular case is that, classic, of the elastic unloading: if the quantity

$$\frac{\Sigma^{*2}_{eq}}{\Sigma'^2_1}+2\tilde{p}'\ sinh\left(\frac{3}{2}\frac{\Sigma^*_m}{\Sigma'_2}\right)-1-\tilde{p}'^2 \tag{71}$$

(or the analogous quantities if work hardening is kinematic or mixed) is negative, there is discharge, therefore $\Delta\varepsilon_{eq} = \Delta\varepsilon^{p}_{m} = \Delta\varepsilon_{m} = 0, \Delta f_1 = 0$ and there is no need to perform constraint correction. The second is that of the closing of the cavities. Examining this possibility requires comparing the porosity to its initial value f_0. Given the explicit nature of the algorithm used with respect to this parameter, it makes sense to test not the true porosity f' at time $t + \Delta t$ (which is known only at the end of the computation, after the convergence of the double iterative process), but on its approximation $\tilde{f}'$ given by Eq. (36). The reclosing test is therefore the conjunction of the inequalities $\tilde{f}' \leq f_0$ and $sh < 0$, where sh denotes the hyperbolic *sine* of $\frac{3}{2}\frac{\Sigma^{*}\mathrm{m}}{\Sigma'_2}$ or analogous quantities. If this test is carried out, it is considered that the criterion is that of Von Mises and the flow rule, that naturally associated $\left(\Leftrightarrow \tilde{p}' = \tilde{p}'' = 0\right.$ in the previous equations).

The third special case, in a way diametrically opposed to the previous one, is that of total damage, that is to say the one where the porosity becomes so high that p exceeds 1. In this case, the material is totally ruined. It is then enough, instead of performing the constraint correction as indicated above, to cancel $\mathbf{\Sigma}'$. The calculation of the evolution of the hardening parameters is not necessary, the material remaining by hypothesis ruined later,[6] but it is necessary all the same to continue to calculate the local increment of porosity Δf_1, because it influences, in the event of relocation of the damage, the evolution of the porosity at the close points, the knowledge of which remains *a priori* necessary because these points may not themselves be ruined.

The last special case is that of sudden germination (decohesion of the metallic matrix around the inclusions). To treat this case, it is necessary to maintain at 0 the porosity (even, in the case of the delocalization of the damage, if that of the neighboring points already evolves) as long as the criterion Eq. (13) is not carried out. As soon as it becomes so, it is necessary to set $f = f_0$ and to continue the calculation normally.

3.5. Numerical treatment of the damage delocalization

This procedure uses an array AF(I, J). The first index varies from 1 to 6, the second from 1 to the total number of Gauss points concerned by the delocalization (it identifies the Gauss point). The meanings of the different quantities AF(I, J) are as follows:

- AF(1, J), AF(2, J), AF(3, J): Current coordinates of Gaussian point J;
- AF(4, J): Local porosity increment (between times t and $t + \Delta t$) at the Gaussian point J;
- AF(5, J): Real increment (after convolution) of porosity at the Gaussian point J;
- AF(6, J): Gauss point weight (for integration).

The calculation procedure is as follows: at all the iterations and for all the Gauss points, the program is used to calculate the coordinates and the weight of the Gauss point and stores them in AF(1 − 3, J) and AF(6, J). It also calls the sub-program, which evaluates the local porosity increment; the latter is stored in AF(4, J). Once the convergence on the nodal imbalances has been obtained, another program is called which, thanks to a double loop on the Gauss points, performs the convolution operation. The actual porosity increment at the point J, stored in AF(5, J), is transmitted to a program, which performs the final operation of calculating and storing the porosity at time t and $t + \Delta t$.

3.6. Correction of the mean part of the deformation rate

The first tests of the program made appear a difficulty which is not specific to the ductile fracture but arises in a general way in elastoplasticity large deformations. This difficulty consists of an inaccuracy in the calculation of the average part of the rate of total deformation (which affects, via the law of elasticity or the law of plastic flow in the case of the ductile damage, the average stress). The origin of this inaccuracy is as follows. Between two times of calculation t and $t + \Delta t$, the algorithm employed uses a formulation linearized compared to the increment of displacement $\Delta\mathbf{u}$; thus the increment of deformation is given by the formula:

$$\Delta d_{ij} = \frac{1}{2}\left(\frac{\partial \Delta \mathrm{u_i}}{\partial \mathrm{x_j}} + \frac{\partial \Delta \mathrm{u_j}}{\partial \mathrm{x_i}}\right) \tag{72}$$

where the $\mathrm{x_i}$ designates the coordinates at time $t + \Delta t$. Similarly, the average strain is taken equal to

$$\Delta d_{\mathrm{m}} = \frac{1}{3}\frac{\partial \Delta \mathrm{u_i}}{\partial \mathrm{x_i}}. \tag{73}$$

The problem stems from the fact that due to quasi-incompressibility (compressibility is only due to elasticity and possibly damage, which, at least at the beginning of mechanical history, is weak), Δd_{m} is small compared to each of Δd_{ij}. As a result, the neglected second-order terms in the above formulas, although indeed small compared to each of $\partial \Delta \mathrm{u_i} \Big/ \partial \mathrm{x_j}$, are not small compared to the sum $\partial \Delta \mathrm{u_i} \Big/ \partial \mathrm{x_i}$, and it is therefore illegal to delete them in the expression of Δd_{m}.

[6] For this purpose, in the program, f is prevented from decreasing again if p has reached or exceeded the value 1.

We have therefore decided to calculate the deviatoric part $\Delta\mathbf{e}$ of the total deformation increment using a linearized formula, but its average part Δd_{m} exactly. To do this, we evaluate the variation in volume between the instants t and $t+\Delta t$ using the exact formula:

$$\frac{\mathcal{V}}{\mathcal{V}+\Delta\mathcal{V}} = det\left(\delta_{ij} - \frac{\partial \Delta u_i}{\partial x_j}\right) \tag{74}$$

[7] and then Δd_{m} by

$$3\Delta d_{\mathrm{m}} = \frac{\Delta\mathcal{V}}{\mathcal{V}} = \frac{1}{det\left(\delta_{ij} - \frac{\partial \Delta u_i}{\partial x_j}\right)} - 1 \tag{76}$$

This formula, linearized with respect to $\Delta\mathcal{V}\Big/\mathcal{V}$, poses no problem because $\Delta\mathcal{V}\Big/\mathcal{V}$ is effectively small (only the expansion of $\Delta\mathcal{V}\Big/\mathcal{V}$ to the first order according to the $\partial\Delta u_i\Big/\partial x_j$, that we are careful here not to perform, would pose one).

4. Numerical implementation at finite strain

Writing constitutive equations for elastic-plastic large deformation for metals requires a temporary objective derivative (i.e. independent of the two references in which it is evaluated); this derivative intervenes on one hand in the hypo-elasticity law, and on the other one, in the case of kinematics hardening, in the evolution equation of the center of the domain of elasticity.

In the formulation adopted in many finite elements codes, the derivative chosen was the most simple one, the Jaumann Derivative, defined by (considering for example the derivative of the Cauchy stress tensor $\mathbf{\Sigma}$):

$$\hat{\mathbf{\Sigma}} = \dot{\mathbf{\Sigma}} + \mathbf{\Sigma}.\mathbf{\Omega} - \mathbf{\Omega}.\mathbf{\Sigma} \tag{77}$$

where $\mathbf{\Omega}$ defines the rate of rotation given by

$$\mathbf{\Omega} = \frac{1}{2}\left(\nabla_{\mathbf{x}}\mathrm{U} - {}^{t}\nabla_{\mathbf{x}}\mathrm{U}\right) \Leftrightarrow \Omega_{ij} = \frac{1}{2}\left(\frac{\partial \mathrm{U}_i}{\partial x_j} - \frac{\partial \mathrm{U}_j}{\partial x_i}\right) \tag{78}$$

(x, current position vector; U the velocity vector). The use of this derivative to calculate the behavior in simple shear gives rise to oscillations of the shear stress as a function of the strain. Although this prediction only concerns very large deformations and, consequently, no experiment has ever come to demonstrate its unrealistic character, it is considered unsatisfactory, at least for the spirit, by many authors. It therefore seems desirable, to prevent criticism which is always possible, to offer the user of our finite element code the possibility of using another derivative not subject to this drawback.

A possible choice, suggested by Fressengeas and Molinari [27,28], is to adopt the Green-Naghdi derivative defined by the same formula as in Eq. (77) above, but $\mathbf{\Omega}$ being given here by

$$\mathbf{\Omega} = \dot{\mathbf{R}}.\mathbf{R}^{-1} \tag{79}$$

where $\mathbf{R}$ denotes the polar decomposition of the gradient of deformation $\mathbf{F}$. We recall that this term denotes a multiplicative decomposition of $\mathbf{F}$ of the form

$$\mathbf{F} = \mathbf{R}.\mathbf{S} \tag{80}$$

where $\mathbf{R}$ is a rotation matrix and $\mathbf{S}$ is a symmetric matrix $\left({}^{t}\mathbf{S} = \mathbf{S}\right)$. Similarly, $\mathbf{F}$ admits the decomposition

$$\mathbf{F} = \tilde{\mathbf{S}}.\mathbf{R} \tag{81}$$

where $\tilde{\mathbf{S}}$ is another symmetric matrix but $\mathbf{R}$ is the same rotation matrix. The matrices $\mathbf{R}, \mathbf{S}, \tilde{\mathbf{S}}$ are defined unequivocally if it is specified that they vary continuously and that at the initial time (where $\mathbf{F} = \mathbf{I}$), $\mathbf{R} = \mathbf{S} = \tilde{\mathbf{S}} = \mathbf{I}$.

We describe here the numerical implementation associated with the choice of this derivative and integrated in our finite element code.

[7] It would seem more natural to use the formula instead:

$$\frac{\mathcal{V}+\Delta\mathcal{V}}{\mathcal{V}} = det\left(\delta_{ij} + \frac{\partial \Delta u_i}{\partial X_j}\right) \tag{75}$$

where the x_j denotes the coordinates at time t. But this would be more delicate because in practice, when passing from instant t to instant $t+\Delta t$, only the coordinates $\left(x_j\right)$ at time $t+\Delta t$ (and associated shape functions), and not of those $\left(X_j\right)$ at time t.

4.1. Calculations of $\mathbf{F}^{-1}$ at the times t and $t+\Delta t$

The whole problem is to calculate the discretized Green-Naghdi rotation rate $\mathbf{\Omega}\Delta t \equiv \Delta\mathbf{\Omega} = \Delta\mathbf{R}\mathbf{R}^{-1}$ (we then deduce for example the discretized Molinari stress rate $\Delta\mathbf{\Sigma} \equiv \Delta\mathbf{\Sigma} + \mathbf{\Sigma}\Delta\mathbf{\Omega} - \Delta\mathbf{\Omega}\mathbf{\Sigma}$). This requires calculating the rotations $\mathbf{R}(t) \equiv \mathbf{R}$ and $\mathbf{R}(t+\Delta t) \equiv \mathbf{R}'$ (or $\mathbf{R}$ and $\Delta\mathbf{R} = \mathbf{R}' - \mathbf{R}$), and for this the deformation gradients $\mathbf{F}(t) \equiv \mathbf{F}$ and $\mathbf{F}(t+\Delta t) \equiv \mathbf{F}'$.

The formula giving $\mathbf{F}'$ is written:

$$\mathbf{F}' = \frac{\partial \mathrm{x}'}{\partial \mathrm{X}} = \mathbf{I} + \frac{\partial \mathrm{u}'}{\partial \mathrm{X}} \Leftrightarrow \mathrm{F}'_{\mathrm{ij}} = \delta_{\mathrm{ij}} + \frac{\partial \mathrm{u}'_{\mathrm{i}}}{\partial \mathrm{X}'_{\mathrm{j}}} \tag{82}$$

where X denotes the position vector at the time 0, x' the position vector at time $t+\Delta t$ and u' the displacement vector at this time ($\mathrm{u}' = \mathrm{x}' - \mathrm{X}$). However, the use of this formula poses a problem because, when going from the time t to the time $t+\Delta t$, we only have the shape functions relative to the final coordinates x'_{i} (which prohibits evaluating the derivatives with respect to the initial coordinates X_{i}). It is therefore more convenient to calculate the inverse of $\mathbf{F}'$ using the formula

$$\mathbf{F}'^{-1} = \frac{\partial \mathrm{X}}{\partial \mathrm{x}'} = \mathbf{I} - \frac{\partial \mathrm{u}'}{\partial \mathrm{x}'} \Leftrightarrow \mathrm{F}'^{-1}_{\mathrm{ij}} = \delta_{\mathrm{ij}} - \frac{\partial \mathrm{u}'_{\mathrm{i}}}{\partial \mathrm{X}'_{\mathrm{J}}} \tag{83}$$

Of course, it is in fact the discretized version of this equation that we use:

$$\mathrm{F}'^{-1}_{\mathrm{ij}} = \delta_{\mathrm{ij}} - \sum_{\mathrm{p}} \frac{\partial \mathrm{N}_{\mathrm{p}}\left(\mathrm{x}'\right)}{\partial x'_{\mathrm{j}}} \mathrm{u}'_{\mathrm{i}}(\mathrm{p}) \tag{84}$$

where the sum is extended to all the nodes of the mesh to which the considered (Gaussian) point belongs, and where $\mathrm{N}_{\mathrm{p}}\left(\mathrm{x}'\right)$ and $\mathrm{u}'(\mathrm{p})$ denote respectively the shape function associated with the node p and the displacement (at time t + Δt) of this node. The inverse of $\mathbf{F}$ can be evaluated as follows:

$$\begin{aligned} &\mathbf{F}^{-1} = \frac{\partial \mathrm{X}}{\partial \mathrm{x}} = \frac{\partial \mathrm{X}}{\partial \mathrm{x}'}.\frac{\partial \mathrm{x}'}{\partial \mathrm{x}} = \mathbf{F}'^{-1}.\left(\mathbf{I} + \frac{\partial \Delta \mathrm{u}}{\partial \mathrm{x}}\right).\mathbf{F}'^{-1}.\left(\mathbf{I} + \frac{\partial \Delta \mathrm{u}}{\partial \mathrm{x}'}\right) \\ &\Leftrightarrow F^{-1}_{\mathrm{ij}} = F'^{-1}_{\mathrm{ik}}.\left(\delta_{\mathrm{kj}} + \frac{\partial \Delta \mathrm{u}_{\mathrm{k}}}{\partial x'_{\mathrm{j}}}\right) \end{aligned} \tag{85}$$

where x denotes the position vector at the time t and Δu the increment of displacement between the times t and $t+\Delta t$ ($\Delta\mathrm{u} = \mathrm{u}' - \mathrm{u}$, u ≡ move at the time t). The error made by replacing $\partial\Delta\mathrm{u}\Big/\partial\mathrm{x}$ by $\partial\Delta\mathrm{u}\Big/\partial\mathrm{x}'$ is negligible because of the second order in Δt whereas the algorithm used is of the first order. The derivatives $\partial\Delta\mathrm{u}_{\mathrm{k}}\Big/\partial\mathrm{x}'_{\mathrm{j}}$ are of course still evaluated here using the gradients of the shape functions (relative to the coordinates x'_{i}).

4.2. Two dimensional case

We must now calculate $\mathbf{R}$ and $\mathbf{R}'$, or $\mathbf{R}$ and $\Delta\mathbf{R}$, and the discretized rotation rate $\Delta\mathbf{\Omega}$. We are going to distinguish here the two-dimensional and three-dimensional cases, because we will not proceed in the same way in the two cases (direct calculation of $\mathbf{R}$ and $\mathbf{R}$ without storage in the two-dimensional case, calculation of $\mathbf{R}$ and $\Delta\mathbf{R}$ with storage of $\mathbf{R}$ in the three-dimensional case). Let us consider first the two-dimensional case. Since we do not know $\mathbf{F}$ and $\mathbf{F}'$ directly but their inverses, it is convenient to consider the polar decompositions of these inverses:

$$\mathbf{F}^{-1} = \mathcal{R}.\mathcal{S} = \tilde{\mathcal{S}}.\mathcal{R},\ \mathbf{F}'^{-1} = \mathcal{R}'.\mathcal{S}' = \tilde{\mathcal{S}}'.\mathcal{R}' \tag{86}$$

where $\mathcal{R}$ and $\mathcal{R}'$ are the rotation matrices, $\mathcal{S}, \tilde{\mathcal{S}}, \mathcal{S}', \tilde{\mathcal{S}}'$ symmetric matrices. The quantities $\mathcal{R}$ and $\mathcal{R}'$ are none other than the inverses of $\mathbf{R}$ and $\mathbf{R}'$: indeed, for $\mathbf{F}$ for example, we have:

$$\mathbf{F}^{-1} = \tilde{\mathcal{S}}.\mathcal{R} \Rightarrow \mathbf{F} = \mathcal{R}^{-1}.\tilde{\mathcal{S}}^{-1}; \tag{87}$$

the comparison with Eq. (81) and the uniqueness of $\mathcal{R}$ and $\mathcal{S}$ show that $\mathcal{R}^{-1} = \mathbf{R}$. If we know how to calculate $\mathcal{R}$ and $\mathcal{R}'$, we can easily deduce the discretized rotation rate:

$$\Delta\mathbf{\Omega} = \mathbf{\Delta R}.\mathbf{R^{-1}} \cong \mathbf{\Delta R}.\mathbf{R'^{-1}} = \left(\mathbf{R}' - \mathbf{R}\right).\mathbf{R'^{-1}} = \mathbf{1} - \mathbf{R}.\mathbf{R'^{-1}} = \mathbf{1} - \mathcal{R}^{-1}.\mathcal{R}'. \tag{88}$$

The problem is therefore reduced to the calculation of the rotations $\mathcal{R}$ and $\mathcal{R}'$ or to that, equivalent, of the matrices $\mathcal{S}$ and $\mathcal{S}'$, of the polar decompositions of $\mathbf{F}^{-1}$ and $\mathbf{F}'^{-1}$. Consider for example that of $\mathbf{F}^{-1}$. Let us introduce the matrix of dilatations (symmetric and known)

$$\mathbf{C} = {}^{t}\mathbf{F}^{-1}.\mathbf{F}^{-1}. \tag{89}$$

Thus, we have

$$\mathbf{C} = {}^t(\mathcal{R}.\mathcal{S}).\mathcal{R}.\mathcal{S} = {}^t\mathcal{S}\,{}^t\mathcal{R}.\mathcal{R}.\mathcal{S} = \mathcal{S}^2. \tag{90}$$

Thus $\mathcal{S}$ appears as the square root of $\mathbf{C}$. This square root is uniquely defined given the requirements that it is symmetric, a continuous function of time (like $\mathbf{C}$) and identical to the identity at the initial time. Let assume that:

$$\mathbf{C} = \begin{bmatrix} r & s \\ s & c \end{bmatrix}; \mathcal{S} = \begin{bmatrix} \alpha & \beta \\ \beta & \gamma. \end{bmatrix} \tag{91}$$

The matrix equation $\mathbf{C} = \mathcal{S}^2$ is then written:

$$\begin{cases} \alpha^2 + \beta^2 & = r \\ \beta(\alpha + \gamma) & = s\ . \\ \beta^2 + \gamma^2 & = c \end{cases} \tag{92}$$

In addition, from the equality $det(\mathbf{C}) = (det(S))^2$ reads:

$$\Delta \equiv rc - s^2 = (\alpha\gamma - \beta)^2 \Rightarrow \alpha\gamma - \beta^2 = \sqrt{\Delta}, \tag{93}$$

the choice of the sign in front of the radical results from the continuity and that initially, $\Delta = 1, \alpha = \gamma = 1, \beta = 0$. Adding this result to Eq. $(92)_1$ on one hand, Eq. $(92)_3$ on the other hand, we obtain:

$$\begin{cases} \alpha(\alpha + \gamma) = r + \sqrt{\Delta} \\ \gamma(\alpha + \gamma) = c + \sqrt{\Delta} \end{cases} \tag{94}$$

the addition of these equations gives $(\alpha+\gamma)^2 = r+c+2\sqrt{\Delta}$, i.e. $\alpha+\gamma = \sqrt{r+c+2\sqrt{\Delta}}$ given that initially, $r = c = 1, \Delta = 1$, $\alpha = \gamma = 1$. Transferring this result to Eq. (94) and Eq. $(92)_2$, we finally obtain:

$$\begin{cases} \alpha = \dfrac{r + \sqrt{\Delta}}{\sqrt{r + c + 2\sqrt{\Delta}}} \\ \beta = \dfrac{s}{\sqrt{r + c + 2\sqrt{\Delta}}} \\ \gamma = \dfrac{c + \sqrt{\Delta}}{\sqrt{r + c + 2\sqrt{\Delta}}} \end{cases} \tag{95}$$

These equations allow the calculation of $\mathcal{S}$ as a function of $\mathbf{C}$. The expression of $\mathcal{R}$ follows immediately thanks to the formula $\mathcal{R} = \mathbf{F}^{-1}.\mathcal{S}^{-1}$.

4.3. The three dimensional case

We have seen, in the two-dimensional case, that the calculation of $\mathcal{R}$ or $\mathcal{S}$ is equivalent to that of the square root of C, itself fundamentally equivalent to the diagonalization of this matrix. In the two-dimensional case, this results in painless extractions of square roots. In the three-dimensional case, it is a question of solving an equation of the 3^{rd} degree, which is more unpleasant and costly in computing time. We therefore use another, faster method, consisting of an incremental calculation of $\mathbf{R}$ (and $\mathbf{R}'$) and requiring storage, Gauss point by Gauss point, of $\mathbf{R}$. This method would indeed also lead to faster calculations in the two-dimensional case, but its use is not possible in this case because of the need to store $\mathbf{R}$.

4.3.1. Calculation of the rotation from the rotation vector

In fact, the storage of the rotation matrix itself is less economical (9 quantities to store) and redundant, the coefficients being related due to the relationship ${}^t\mathbf{R}.\mathbf{R} = \mathbf{R}.{}^t\mathbf{R} = \mathbf{I}$. The most economical way to proceed[8] consists in storing the 3 components of the rotation vector $\mathbf{V}$ defined by:

$$\mathrm{V} = \Theta \mathrm{v} \tag{96}$$

[8] A classic method is to store the quaternion associated with the rotation; but this quaternion has 4 components instead of 3.

where Θ denotes the angle of rotation and v the unit vector parallel with the axis of rotation. The angle Θ is a priori defined modulo 2π, but it is obvious that we can change the sign of Θ and v without modifying $\mathbf{R}$; there is therefore uniqueness of Θ and v only if it is specified that Θ is in the interval $[0, \pi]$.

The first problem that arises is therefore to reconstruct the rotation matrix $\mathbf{R}$ from the rotation vector V. For this, let us calculate the image, by the rotation $\mathbf{R}$, of any vector W. The projection of W on the axis of rotation is $(\mathrm{v}.\mathrm{W})\,\mathrm{v} = \frac{1}{\Theta^2}(\mathrm{V}.\mathrm{W})\,\mathrm{V}$; this projection is rotation invariant. The projection of W on the plane perpendicular to the axis of rotation is $\mathrm{W}' = \mathrm{W} - \frac{1}{\Theta^2}(\mathrm{V}.\mathrm{W})\mathrm{V}$; after rotation, this projection becomes:

$$\cos\Theta\mathrm{W}' + \sin\Theta\mathrm{v}\wedge\mathrm{W}' = \cos\Theta\left[\mathrm{W} - \frac{1}{\Theta^2}(\mathrm{V}.\mathrm{W})\mathrm{V}\right] + \frac{\sin\Theta}{\Theta}\mathrm{V}\wedge\left[\mathrm{W} - \frac{1}{\Theta^2}(\mathrm{V}.\mathrm{W})\mathbf{V}\right] \tag{97}$$

$$= \cos\Theta\left[\mathrm{W} - \frac{1}{\Theta^2}(\mathrm{V}.\mathrm{W})\mathrm{V}\right] + \frac{\sin\Theta}{\Theta}\mathrm{V}\wedge\mathrm{W}. \tag{98}$$

In total, W thus becomes, after rotation,

$$\mathbf{R}.\mathrm{W} = \frac{1-\cos\Theta}{\Theta^2}(\mathrm{V}.\mathrm{W})\mathrm{V} + \cos\Theta\mathrm{W} + \frac{\sin\Theta}{\Theta}\mathrm{V}\wedge\mathrm{W}. \tag{99}$$

The components of $\mathbf{R}$ are therefore given, given that $(\mathrm{V}\wedge\mathrm{W})_i = \varepsilon_{ikj}.\mathrm{V}_k\mathrm{W}_j$ where ε denotes the permutation tensor (completely anti-symmetric), by the formula:

$$\mathrm{R}_{ij} = \frac{1-\cos\Theta}{\Theta^2}\mathrm{V}_i\mathrm{V}_j + \cos\Theta\delta_{ij} + \frac{\sin\Theta}{\Theta}\varepsilon_{ikj}\mathrm{V}_k,\ \Theta \equiv ||\mathrm{V}|| \tag{100}$$

4.4. Calculation of the discretized rate of the rotation vector

We now come to the central problem, which is to calculate, from the knowledge of $\mathbf{R}, \mathbf{F}^{-1}, \mathbf{F}'^{-1}$, the discretized rotation rate $\Delta\boldsymbol{\Omega} = \boldsymbol{\Delta}\mathbf{R}.\mathbf{R}^{-1}$, or rather the associated discretized rotation rate vector $\Delta\omega$, defined by:[9]

$$\forall\,\mathrm{W}:\ \Delta\Omega.\mathrm{W} = \Delta\omega\wedge\mathrm{W} \tag{101}$$

From $\mathbf{R}, \mathbf{F}^{-1}, \mathbf{F}'^{-1}$, we easily form the matrices

$$\begin{cases} \Delta\mathbf{M} = \mathbf{R}.\left(\mathbf{F}^{-1} - \mathbf{F}'^{-1}\right) \\ \tilde{\mathbf{S}}^{-1} = \mathbf{R}.\mathbf{F}^{-1} \end{cases} \tag{102}$$

($\tilde{\mathbf{S}}^{-1}$ is none other than the inverse of the matrix $\tilde{\mathbf{S}}$ of the polar decomposition Eq. (81)). Let $\Delta\tilde{\mathbf{S}} = \tilde{\mathbf{S}}' - \tilde{\mathbf{S}}$, where $\tilde{\mathbf{S}}'^{-1}$ denotes the symmetric matrix of the polar decomposition Eq. (81)) at the time $t + \Delta t$.

We have

$$\tilde{\mathbf{S}}'^{-1} = (\tilde{\mathbf{S}} + \Delta\tilde{\mathbf{S}})^{-1} = \left[\tilde{\mathbf{S}}.\left(\mathbf{I} + \tilde{\mathbf{S}}^{-1}.\Delta\tilde{\mathbf{S}}\right)\right]^{-1} \cong \left(\mathbf{I} - \tilde{\mathbf{S}}^{-1}.\Delta\tilde{\mathbf{S}}\right)\tilde{\mathbf{S}}^{-1} \tag{103}$$

Therefore:

$$\begin{aligned} \Delta\mathbf{M} = \mathbf{R}.\left(\mathbf{F}^{-1} - \mathbf{F}'^{-1}\right) &= \mathbf{R}.\left[{}^t\mathbf{R}.\tilde{\mathbf{S}}^{-1} - \left({}^t\mathbf{R} + {}^t\Delta\mathbf{R}\right)\left(\tilde{\mathbf{S}}^{-1} - \tilde{\mathbf{S}}^{-1}\Delta\tilde{\mathbf{S}}.\tilde{\mathbf{S}}^{-1}\right)\right] \\ &\cong \mathbf{R}.\left({}^t\mathbf{R}.\tilde{\mathbf{S}}^{-1}\Delta\tilde{\mathbf{S}}.\tilde{\mathbf{S}}^{-1} - {}^t\Delta\mathbf{R}.\tilde{\mathbf{S}}^{-1}\right) \\ &= \tilde{\mathbf{S}}^{-1}.\Delta\tilde{\mathbf{S}}.\tilde{\mathbf{S}}^{-1} - \mathbf{R}{}^t\Delta\mathbf{R}.\tilde{\mathbf{S}}^{-1} \\ &= \tilde{\mathbf{S}}^{-1}.\Delta\tilde{\mathbf{S}}.\tilde{\mathbf{S}}^{-1} - \mathbf{R}{}^t\Delta\mathbf{R}.\tilde{\mathbf{S}}^{-1} \\ &= \tilde{\mathbf{S}}^{-1}.\Delta\tilde{\mathbf{S}}.\tilde{\mathbf{S}}^{-1} - \mathbf{R}{}^t\Delta\mathbf{R}.\tilde{\mathbf{S}}^{-1} \\ &= \tilde{\mathbf{S}}^{-1}.\Delta\tilde{\mathbf{S}}.\tilde{\mathbf{S}}^{-1} + \Delta\boldsymbol{\Omega}.\tilde{\mathbf{S}}^{-1} \end{aligned} \tag{104}$$

As a consequence

$$\Delta\mathbf{M} - {}^t\Delta\mathbf{M} = \Delta\boldsymbol{\Omega}.\mathbf{S}^{-1} + \tilde{\mathbf{S}}^{-1}.\Delta\boldsymbol{\Omega} \tag{105}$$

Let $\Delta\mathrm{m}$ be the (known) vector associated with the anti-symmetric matrix $\Delta\mathbf{M} - {}^t\Delta\mathbf{M}$. We then have $\Delta\mathrm{M}_{ij} - \Delta\mathrm{M}_{ji} = \varepsilon_{ikj}\Delta\mathrm{m}_k$, and likewise $\Delta\Omega_{ij} = \varepsilon_{ikj}\Delta\omega_k$. The previous equation is therefore written as:

$$\varepsilon_{ikj}\Delta\mathrm{m}_k = \Delta\Omega_{ik}\tilde{S}^{-1}_{kj} + \tilde{S}^{-1}_{ik}\Delta\Omega_{kj} = \varepsilon_{ilk}\Delta\omega_l\tilde{S}^{-1}_{kj} + \tilde{S}^{-1}_{ik}\varepsilon_{klj}\Delta\omega_l \tag{106}$$

Multiplying on the right and on the left by ε_{ijp} we obtain

[9] To some terms in $(\Delta t)^2$, $\Delta\omega = \dot{\mathbf{R}}.\mathbf{R}^{-1}$ is anti-symmetric; to any such matrix $\mathbf{A}$ is associated with a vector a such that $\forall\mathrm{W}, \mathbf{A}.\mathrm{W} = \mathrm{a}\wedge\mathrm{W}$.

$$\begin{aligned}
\varepsilon_{ikj}\varepsilon_{ijp}\Delta m_k &= -\varepsilon_{ijk}\varepsilon_{ijp}\Delta m_k = -2\delta_{kp}\Delta m_k = -2\Delta m_p \\
&= \varepsilon_{ilk}\varepsilon_{ijp}\Delta\omega_l\tilde{S}^{-1}_{kj} + \varepsilon_{klj}\varepsilon_{ijp}\tilde{S}^{-1}_{ik}\Delta\omega_l \\
&= \left(\delta_{lj}\delta_{kp} - \delta_{lp}\delta_{kj}\right)\tilde{S}^{-1}_{kj}\Delta\omega_l + \left(\delta_{kp}\delta_{li} - \delta_{ki}\cdot\delta_{lp}\right)\tilde{S}^{-1}_{ik}\Delta\omega_l \\
&= \tilde{S}^{-1}_{pj}\Delta\omega_j - \tilde{S}^{-1}_{jj}\Delta\omega_p + \tilde{S}^{-1}_{ip}\Delta\omega_i - \tilde{S}^{-1}_{ii}\Delta\omega_p \\
&= 2\tilde{S}^{-1}_{pj}\Delta\omega_j - 2\tilde{S}^{-1}_{jj}\Delta\omega_p \\
&\Rightarrow \Delta m_p = \left[\left(\mathrm{tr}\tilde{\mathbf{S}}^{-1}\right)\delta_{pj} - \tilde{S}^{-1}_{pi}\right]\Delta\omega_j.
\end{aligned} \tag{107}$$

This can be written as:

$$\Delta\mathrm{m} = \left[\left(\mathrm{tr}\tilde{\mathbf{S}}^{-1}\right)\mathbf{I} - \tilde{\mathbf{S}}^{-1}\right].\Delta\omega \tag{108}$$

Thus we can obtain the discretized rotation rate vector $\Delta\omega$ from $\Delta\mathrm{m}$ (i.e. $\Delta\mathbf{M}$) by simply inverting a 3×3 matrix (which is much less expensive in calculation time than a diagonalization):

$$\Delta\omega = \left[\left(\mathrm{tr}\tilde{\mathbf{S}}^{-1}\right)\mathbf{I} - \tilde{\mathbf{S}}^{-1}\right].\Delta\mathrm{m}. \tag{109}$$

We then easily deduce the discretized rotation rate $\Delta\mathbf{\Omega}$ by the formula $\Delta\Omega_{ij} = \varepsilon_{ikj}\Delta\omega_k$.

4.4.1. Calculation of the rate of the rotation vector

The vector $\Delta\omega$ being known, it is necessary to calculate and store the rotation $\mathbf{R}+\Delta\mathbf{R}$ at the time t, or more precisely the vector of rotation $\mathrm{V}+\Delta\mathrm{V}$ at this time t.

An additional advantage here is storing $\mathrm{V}+\Delta\mathrm{V}$ rather than $\mathbf{R}+\Delta\mathbf{R}$. In the second case, since the step Δt is not, numerically, infinitely small, the calculation of $\Delta\mathbf{R}$ inevitably leads to a matrix $\mathbf{R}+\Delta\mathbf{R}$ which is no longer strictly orthogonal. In the first, on the contrary, regardless of the vector $\mathrm{V}+\Delta\mathrm{V}$ calculated, the use, at the next time step, of the formula Eq. (94) with this rotation vector leads to a strictly orthogonal matrix.

To calculate $\Delta\mathrm{V}$, let us rewrite Eq. (99) with the unit vector W instead of the vector $\mathrm{V}=\Theta\mathrm{v}$, and differentiate it with respect to time, W being assumed fixed:

$$\begin{aligned}
&\mathbf{R}.\mathrm{W} = (1-\cos\Theta)(\mathrm{v}.\mathrm{W})\mathrm{v} + (\cos\Theta\mathrm{W} + \sin\Theta\mathrm{v}\wedge\mathrm{W}) \\
&\quad\Rightarrow \Delta\mathbf{R}.\mathrm{W} = \Delta\Theta\sin\Theta(\mathrm{v}.\mathrm{W})\mathrm{v} + (1-\cos\Theta)(\Delta\mathrm{v}.\mathrm{W})\mathrm{v} + (1-\cos\Theta)(\mathrm{v}.\mathrm{W})\Delta\mathrm{v} \\
&\quad - \Delta\Theta\sin\Theta\mathrm{W} + \Delta\Theta.\cos\Theta\,\mathrm{v}\wedge\mathrm{W} + \sin\Theta\Delta\,\mathrm{v}\wedge\mathrm{W}
\end{aligned}$$

Let us apply this relation to the vector $\mathrm{W}=\mathrm{v}$ as $\Delta\mathrm{v}.\mathrm{v}=0$ (v being unitary at any time), we obtain:

$$\begin{aligned}
\Delta\mathbf{R}.\mathrm{v} &= \Delta\Theta.\sin\Theta\mathrm{v} + (1-\cos\Theta)\Delta\mathrm{v} - \Delta\Theta.\sin\Theta\,\mathrm{v} + \sin\Theta(\Delta\mathrm{v})\wedge\mathrm{v} \\
&= (1-\cos\Theta)\Delta\mathrm{v} + \sin\Theta(\Delta\mathrm{v})\wedge\mathrm{v}
\end{aligned}$$

Now, for any vector W, we have $\Delta\mathbf{R}.\mathbf{R}^{-1}.\,\mathrm{W} = \Delta\Omega.\mathrm{W} = \Delta\omega\wedge\mathrm{W}$. For $\mathrm{W}=\mathrm{v}$, we have $\mathbf{R}^{-1}.\mathrm{v}=\mathrm{v}$ (v is carried by the axis of rotation) and therefore $\Delta\mathbf{R}.\mathrm{v} = \Delta\omega\wedge\mathrm{v}$. The previous equation is therefore written as:

$$\Delta\omega\wedge\mathrm{v} = (1-\cos\Theta)\Delta\mathrm{v} + \sin\Theta\,(\Delta\mathrm{v})\wedge\mathrm{v}. \tag{110}$$

Let us take the cross product of this equation and the vector v; taking into account the formula of the double cross product, we obtain:

$$(\Delta\omega.\mathrm{v})\mathrm{v} - \Delta\omega = (1-\cos\Theta)(\Delta\mathrm{v})\wedge\mathrm{v} - \sin\Theta\Delta\mathrm{v}. \tag{111}$$

So we have both:

$$\begin{cases}
(1-\cos\Theta)\Delta\mathrm{v} + \sin\Theta\,(\Delta\mathrm{v})\wedge\mathrm{v} = \Delta\omega\wedge\mathrm{v} \\
-\sin\Theta\Delta\mathrm{v} + (1-\cos\Theta)(\Delta\mathrm{v})\wedge\mathrm{v} = (\Delta\omega.\mathrm{v})\mathrm{v} - \Delta\omega
\end{cases} \tag{112}$$

Solving this system with respect to the unknown quantities $\Delta\mathrm{v}$ and $(\Delta\mathrm{v})\wedge\mathrm{v}$ immediately gives:

$$\begin{aligned}
\Delta\mathrm{v} &= \frac{1}{2}\Delta\omega\wedge\mathrm{v} + \frac{\sin\Theta}{2(1-\cos\Theta)}\Delta\omega - \frac{\sin\Theta}{2(1-\cos\Theta)}(\Delta\omega.\mathrm{v})\mathrm{v} \\
&= \frac{1}{2}\Delta\omega\wedge\mathrm{v} + \frac{1+\cos\Theta}{2\sin\Theta}\Delta\omega - \frac{1+\cos\Theta}{2\sin\Theta}(\Delta\omega.\mathrm{v})\mathrm{v}
\end{aligned} \tag{113}$$

Note that we were thus able to evaluate $\Delta\mathrm{v}$ without calculating $\Delta\Theta$. However, it is $\Delta\mathrm{V}$, and not $\Delta\mathrm{v}$, that we want to know; as $\mathrm{V}=\Theta\mathrm{v}$, we have

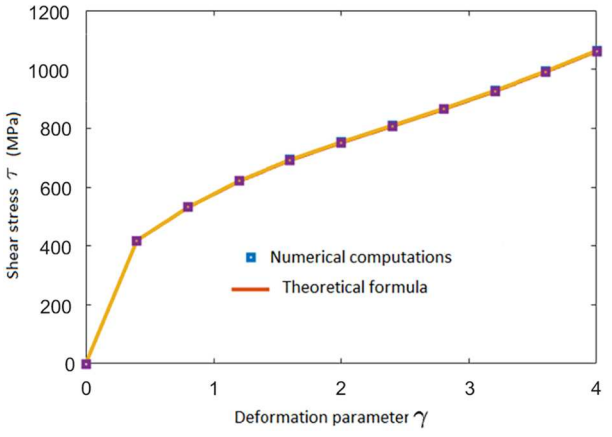

Fig. 1. Shear stress as a function of the deformation parameter.

$$\Delta V = \Delta\Theta.v + \Theta\Delta v = \frac{\Delta\Theta}{\Theta}V + \frac{1}{2}\Delta\omega \wedge V + \frac{\Theta(1+\cos\Theta)}{2\sin\Theta}\Delta\omega - \frac{1+\cos\Theta}{2\Theta\sin\Theta}(\Delta\omega.V)V. \tag{114}$$

To calculate $\Delta\Theta$ as a function of $\Delta\omega$, note that Eq. (94) implies that $tr(\mathbf{R}) = 1 + 2\cos\Theta$; thus, $tr(\Delta\mathbf{R}) = -2\Delta\Theta\sin\Theta$. But, $\left(\Delta\mathbf{R}.\mathbf{R}^{-1}\right)_{ij} = \Delta\Omega_{ij} = \varepsilon_{ikj}\Delta\omega_{\mathbf{k}}$. From there we get

$$\begin{aligned}
&\Delta R_{il} = \left(\Delta\mathbf{R}.\mathbf{R}^{-1}\right)_{ij} R_{j1} = \varepsilon_{ikj}\Delta\omega_k R_{j1} \\
&\Rightarrow \mathrm{tr}(\Delta\mathbf{R}) = \Delta R_{ii} = \varepsilon_{ikj}\Delta\omega_k\left(\frac{1-\cos\Theta}{\Theta^2}V_jV_i + \cos\Theta\delta_{ji} + \frac{\sin\Theta}{\Theta}\varepsilon_{jmi}V_m\right) \\
&= \varepsilon_{ikj}\varepsilon_{jmi}\frac{\sin\Theta}{\Theta}\Delta\omega_k V_m = -2\delta_{km}\frac{\sin\Theta}{\Theta}\Delta\omega_k V_m = -2\frac{\sin\Theta}{\Theta}\Delta\omega.V;
\end{aligned} \tag{115}$$

thus,

$$\Delta\Theta = \frac{1}{\Theta}\Delta\omega.V \tag{116}$$

Transferring this result to the previous expression of ΔV, we finally get

$$\Delta V = \frac{1}{2}\Delta\omega \wedge V + \frac{\Theta(1+\cos\Theta)}{2\sin\Theta}\Delta\omega + \left[\frac{1}{\Theta^2} - \frac{1+\cos\Theta}{2\Theta\sin\Theta}\right](\Delta\omega.V)V \tag{117}$$

This formula allows the incrementation of the vector V. If, after the incrementation, the norm of this vector exceeds π, we correct this last modulo 2πv, i.e. we perform the substitution

$$V \to V - 2\pi v = \left(1 - \frac{2\pi}{||V||}\right)V \tag{118}$$

(which is equivalent to replacing θ by $2\pi - \Theta$ and v by - v).

4.5. *Example: simple shear*

We consider the typical example of a rigid plastic material, with linear kinematic work hardening, subjected to a stress of simple shear. The relations between the initial coordinates X_i and current coordinates x_i are written, for this load:

$$\begin{cases} x_1 = X_1 + \gamma X_2 \\ x_2 = X_2 \\ x_3 = X_3 \end{cases} \tag{119}$$

The expression of the shear stress $\tau \equiv \Sigma_{12}$ as a function of the deformation parameter γ is given by Fresseeneas and Molinari [28].

$$\tau = \frac{\Sigma_0}{\sqrt{3}} + \frac{h}{3}\left[\frac{2\gamma}{1+\gamma^2/4}\ln\left(1+\gamma^2/4\right) + \frac{1-\gamma^2/4}{1+\gamma^2/4}\left(-\gamma + 4\tan^{-1}(\frac{\gamma}{2})\right)\right], \tag{120}$$

where Σ_0 and h denotes the initial elastic limit and the slope of work hardening in a simple tensile test.

Fig. 1 and Table 1 show the comparison of the results obtained numerically (with $\Sigma_0 = 500, h = 1000$ and $E = 2000000$: quasi-rigid material) and those deduced from the formula Eq. (120). The agreement is excellent.

Table 1
Comparisons of numerical calculations vs. theoretical predictions for the simple shear problem.

γ	τ: Numerics (MPa)	τ: Eq. (120) (MPa)
0	0	0
0.4	418.67	418.60
0.8	531.79	531.20
1.2	621.57	620.40
1.6	692.44	690.84
2.0	752.62	750.78
2.4	809.17	807.23
2.8	866.65	864.69
3.2	927.52	925.61
3.6	992.88	991.05
4.0	1063.10	1061.33

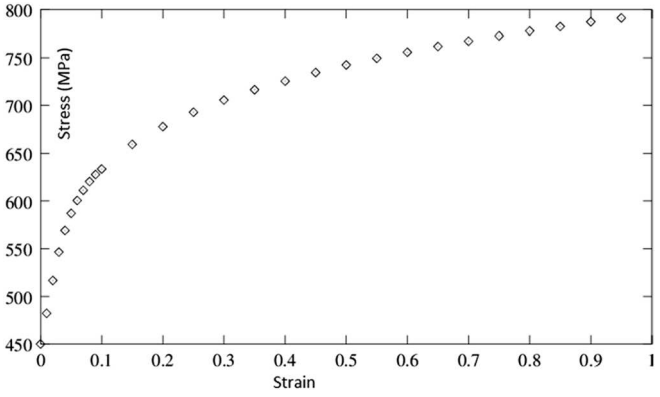

Fig. 2. Experimental stress vs. strain curve for the 16 MND5 steel.

We also compared the theoretical and numerical values of Σ_{11}; the agreement is again excellent. The above comparison is for the two-dimensional option; a comparable agreement is obtained in the three-dimensional option, but not shown here.

5. Applications

5.1. Generalities

We will simulate Mudry's [20] fracture test on a pre-notched and pre-cracked round bars (TA15, TA30, and TA50) made of A508 Class 3 or 16MND5 steel. The available experimental results for comparison concern the low-alloy steel 16MND5, which is used in the fabrication of nuclear reactor vessels. For this steel, the Young's modulus is $E = 203,000$ MPa, the Poisson's ratio is $\nu = 0.3$, and the initial yield strength in uniaxial tension is $\Sigma_y = 450$ MPa.

Numerical simulations were carried out using the finite element code Systus®. In each simulation, the value of the Tvergaard parameter $q = 4/e = 1.47$ was used, as determined by Perrin and Leblond [29] using a "differential" scheme. The other damage parameters depend on the considered material and will be provided later.

The objectives of these simulations, let us recall, are twofold: first, to verify the independence of the numerical results with respect to spatial discretization, and second, to study the practical effectiveness of isotropic and kinematics methods in terms of their ability to reproduce experimental results.

The constitutive relationship of this material is deduced from rational stress-strain curves. The stress-strain curve at 100 °C is well represented by the empirical law:

$$\sigma = 795\varepsilon_p^{0.01},$$

as schematically shown in Figure 2. The elastic part is not represented as it can be neglected without significantly affecting the overall mechanical behavior of the material.

The initial porosity value, denoted as f_0, for this steel, is determined based on a study conducted by Murdy and Rousselier [20], which takes into account the chemical composition and inclusion state. This value is derived from the sulfur and manganese content of the material as well as the average dimensions of the inclusions. The determined value is 0.00016.

Additionally, three damage parameters are included: f_c representing the "critical" porosity for the onset of coalescence, δ as the accelerator factor for cavity growth, and b as the value of the characteristic length scale. These parameters can be adjusted for each simulation, and their respective values are listed in Table A.2.

Depending on the specific case, either isotropic, kinematic, or mixed isotropic-kinematic hardening will be employed to model the inelastic behavior. For one-off or pulsating loading cases, isotropic hardening is considered appropriate and relatively straightforward to implement in a model. In contrast, kinematic hardening models allow for the simulation of fully cyclic behavior but do not account for cyclic hardening and softening effects. If these factors are significant, it is recommended to use mixed-mode or combined models, as they offer the inclusion of these effects in the constitutive material behavior, providing a more comprehensive representation of the physical phenomena.

Due to the limited availability of experimental data for the steels under investigation in these studies, our focus will be solely on isotropic hardening, as it is the only approach for which experimental data are available.

Achieving convergence for the global elasto-plastic iterations posed challenges. In order to maintain the quadratic convergence rate of the global Newton iterations, it becomes necessary to incorporate stiffness tangent moduli, especially for last-scale fracture problem simulations. The calculation of these tangent moduli is a highly intricate endeavor, particularly when dealing with constitutive models of complex nature. The derivation of these moduli is provided in Appendix B for both the Gurson model and the Perrin's models.

5.2. Numerical simulation of tensile axisymmetric pre-notched and pre-cracked specimens

We will analyze three homothetical pre-cracked axisymmetric tensile specimens — TA15, TA30, and TA50 —designed from A508 Cl.3 steel, with corresponding diameters of 15 mm, 30 mm, and 50 mm, respectively. These specimens underwent fracture tests, and the experimental results were meticulously documented by Rousselier and Mudry [20]. To maintain consistency across all cases, a uniform minimum element size of 0.2 mm was employed.

Leveraging the symmetry inherent in these structures about the horizontal mid-plane, our analysis focuses solely on the upper halves of the specimens. The dimensions of the specimens, including semi-height and radius, are as follows: TA15 (22.5 mm and 7.5 mm), TA30 (45 mm and 15 mm), and TA50 (75 mm and 25 mm). Notably, the central notch within the meridian plane exhibits a triangular shape, featuring a half-opening angle of 30° and varying depths of 2.5 mm (TA15), 5 mm (TA30), or 8.3 mm (TA50).

Concealed within the figure, a fatigue pre-crack emerges from the notch root with lengths of 0.9 mm (TA15), 1.7 mm (TA30), and 2.85 mm (TA50). From the tip of this pre-crack, a crack develops and propagates towards the axis of rotational symmetry. This pre-crack, although imperceptible in the visual representation, plays a crucial role in the overall structural behavior and will be a focal point of our computational investigation.

General meshes of the three specimens are shown in Fig. 3. The advantage is taken of symmetry about the horizontal mid-plane to mesh only the upper half of the structure. Fig. 4 shows enlarged views of the central region of the TA30 specimen. Near the crack tip of the initial fatigue pre-crack, identical discretizations are used to ensure consistent representation of the initial blunting of the crack, see Fig. 5. This avoids introducing irrelevant differences in the load-displacement curves that could interfere with the study of mesh sensitivity (for instance) due to the constitutive model's softening behavior.

To refine the modeling of intense stress and strain gradients in the crack tip region, a radiant mesh design consisting of four meshes is utilized. These four meshes employ two degenerated quadrilateral elements and two triangular elements, with their intermediate nodes pulled back to a quarter of the distance from the element face. The role of the quadrilateral elements is to facilitate crack tip opening and propagation.

Figures [8, 7, 9] compare the load–displacement curve generated by the model with experimental results for the three specimens. The figures demonstrate that the predicted results mirror pretty well the experimental results when the delocalization technique is applied to the log of the damage parameter. In fact, Enakoutsa et al. [8] have demonstrated that applying a simple delocalization technique on the damage parameter results in excessive smoothing of the porosity in the ligament near the crack type, which yields an earlier drop of the load vs. displacement curve, in contradiction with the experiments.

In our quest to elucidate and contextualize the inherent drawback, a meticulous examination of the obtained results has been undertaken, with a specific focus on unraveling the intricacies of damage distribution within the meshes preceding the crack tip. This analytical endeavor has brought to light a striking incongruity between the initially anticipated scenario and the actual observed behavior.

Contrary to our initial expectations, the initiation of damage does not conform to a linear, sequential progression along the ligament. Instead, it chooses an unpredictable course, manifesting almost simultaneously at various discrete points within the ligamentous structure, as vividly illustrated in the accompanying Fig. 6b. This unexpected and non-sequential initiation of damage poses a significant departure from the theoretical framework we had envisioned.

As a direct consequence of this unanticipated phenomenon, the growth rate of damage within the ligament undergoes an intriguing shift, characterized by a discernible deceleration. This deceleration, in turn, culminates in the abrupt rupture of the ligament. The sudden rupture, far from the anticipated gradual progression, brings about an exceptionally rapid propagation of the crack. This stark deviation from our initially hypothesized behavior is not only intriguing but also holds profound implications for the overall structural integrity and failure mechanisms.

It is crucial to underscore that this unanticipated rupture and rapid crack propagation significantly diverge from the behavior predicted by our theoretical model. This divergence is particularly noteworthy when compared to the findings derived from experimental observations, where a more gradual and sequentially progressing initiation of damage is typically observed. The stark contrast between our theoretical expectations and the empirical reality emphasizes the need for a nuanced reassessment of our initial assumptions and computational models, prompting a deeper exploration of the underlying factors influencing this intricate interplay of damage initiation, propagation, and rupture in the ligamentous structure.

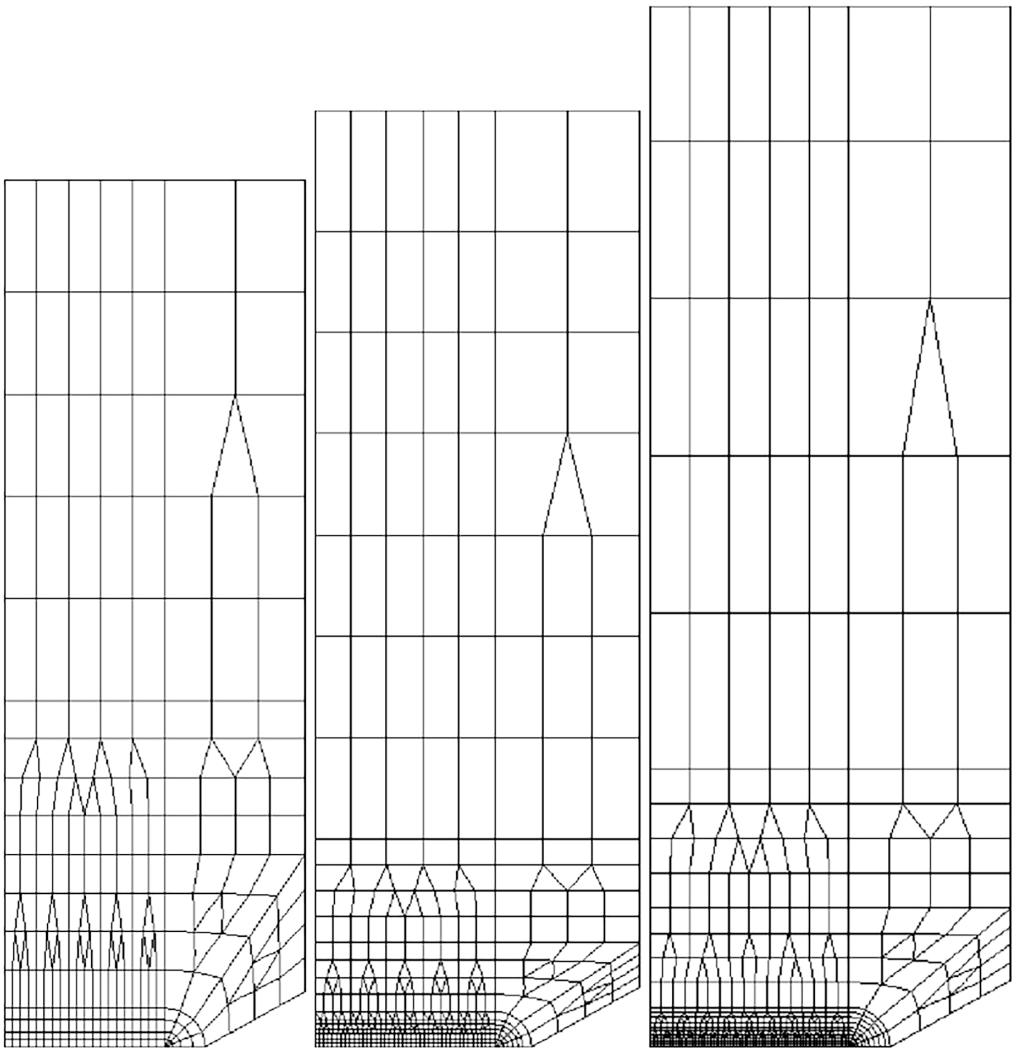

Fig. 3. Meshes of TA pre-cracked specimens - Minimum elements 200 microns.

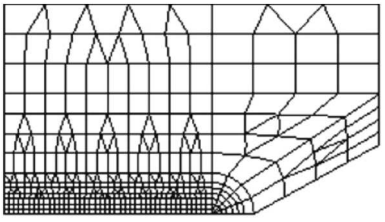

Fig. 4. Zoom of the mesh of the TA30 specimen – Minimum element size 200 microns. Exclusive focus on the TA30 Mesh zoom – out presentation.

The outcomes achieved through the application of the logarithmic convolution method stand resilient against the drawbacks previously mentioned. Indeed, as pointed out in Enakoutsa et al. [8], these limitations stem directly from the diffusive nature inherent in the original nonlocal evolution equation of the damage, inevitably resulting in the potential for unlimited smoothing of the damage. The unique feature of logarithmic delocalization of the damage parameter sets it apart from a diffusion equation, offering a distinct advantage. Consequently, it is anticipated that this approach will enhance the accuracy of numerical predictions compared to those obtained using the original delocalization method.

The findings stemming from the integration of logarithmic delocalization for damage within our study not only serve to accurately portray the initiation of damage in the meshes preceding the crack tip but also unravel a multifaceted narrative surrounding the dynamic heterogeneity characterizing the distribution of damage within the ligament over time. This nuanced evolution in damage

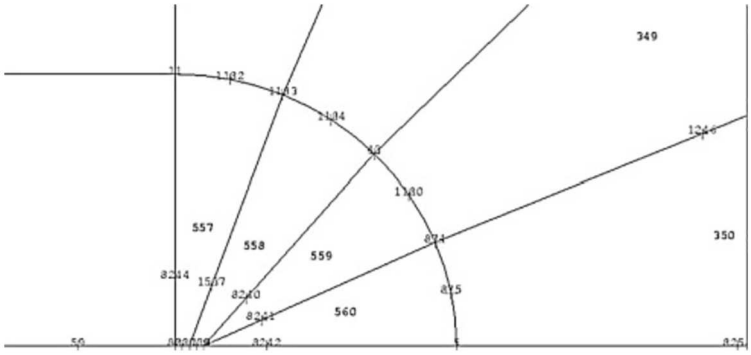

Fig. 5. Mesh discretization near the crack tip with four meshes the intermediates nodes of which are pulled back to the quarter of the distance of the mesh face. Note the ligament ahead the crack tip is made of strictly identical elements.

distribution becomes particularly evident when examining the graphical representations provided in both Fig. 6c and Fig. 6a, where the intricate interplay of variables is elucidated within the specific framework of the LPD local model.

The dynamic heterogeneity observed over time manifests in a progressive breakdown of the ligament, painting a detailed picture of how damage propagates and evolves in a non-uniform manner. This revelation not only enhances our understanding of the intricate mechanics at play but also underscores the significance of considering temporal aspects when analyzing damage evolution.

Furthermore, the novel delocalization method employed in our study demonstrates a remarkable capability in capturing the subtle intricacies associated with the gradual decline of force beyond its peak value. This precision in representing the force dynamics provides valuable insights into the mechanical behavior of materials under stress and contributes to the refinement of predictive models for structural integrity.

In essence, the comprehensive analysis presented here showcases the intricate relationship between logarithmic delocalization, damage initiation, dynamic heterogeneity, and force decline, shedding light on the complex interdependencies that govern material behavior in the context of structural mechanics.

5.3. Simulation of a compact tension (CT) specimen

In this section, we evaluate the effectiveness of the numerical implementation method in replicating the fracture test conducted by Devaux and Mottet [30]. The test involved a CTJ 25 specimen, made of 16MND5 steel stainless steel, which was deformed under plane strain conditions. The CTJ 25 specimen has dimensions of 50 mm (width), 50 mm (height), and 25 mm (thickness). A rectangular notch with a width of 2 mm is located on the top surface. However, as we move towards the notch root, the shape of the notch transitions into a triangular form, with an opening angle of 60°. It is important to note that a fatigue pre-crack, not visible in the figure, with a length of 1.34 mm originates from the notch root.

The discretized geometry of the specimen is illustrated in Fig. 10. To simplify the modeling process, we take advantage of the specimen's symmetry about the vertical mid-plane and only simulate its right half. The triangle in the mesh design of the specimen represents a wedge idealized as an elastic body having the same elastic properties as the actual material. The center of the wedge is the center of the hole machined in the CT specimen. The specimen is loaded via an imposed vertical displacement applied on the center of a wedge.

In this study, we utilize a single 2D mesh since a comprehensive analysis of mesh sensitivity was conducted in the simulations of TA pre-cracked specimens, as described in previous works by Enakoutsa et al. and Enakoutsa [8,9]

During the experiment, the use of lateral central triangular notches and the opening angle ensured that the region where the crack propagated exhibited nearly plane strain conditions, allowing for a two-dimensional simulation. However, because the assumption of perfect plane strain in such a simulation is not entirely accurate, when comparing the simulation results to the experimental data, it is necessary to adjust the applied experimental force by dividing it by an "equivalent thickness" of the specimen, which slightly deviates from the actual thickness. This matter was extensively investigated by Brosse [31], who determined a "best value" of 10.3 mm for this equivalent thickness, which is adopted in this study. The values of the material parameters are provided in Table A.2 in the Appendix section.

Fig. 11 shows the experimental load–displacement curve (in the black points) together with the numerical ones obtained with the inclusion of the kinematics hardening and isotropic hardening. The simulations show that the results with the inclusion of the kinematics hardening (the results are not shown here) do not change with respect to the isotropic hardening due to the simple tension loading conditions we apply to obtain the numerical results. Also, the results of the numerical simulations with the nonlocal model (first version) present an excessive smoothing of the porosity in the ligament ahead of the crack tip which leads to an abrupt drop of the load-displacement curve; this can be fixed by using the ln of the evolution equation of the porosity (see Fig. 11) However, the discrepancy between the numerical predictions generated by the modified nonlocal Gurson's model (with isotropic hardening) and the actual experimental outcomes is undeniably significant, demanding an immediate attention. Nevertheless, this disparity can be decisively mitigated through judicious adjustments to the parameters f_c, representing the porosity value at the onset of coalescence, and the cavities growth accelerator factor δ, respectively, leaving no room for compromise.

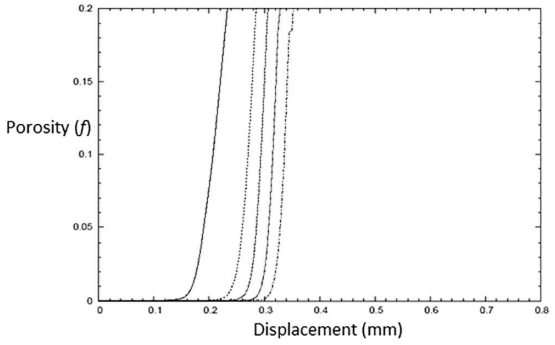

(a) LPD model with local porosity

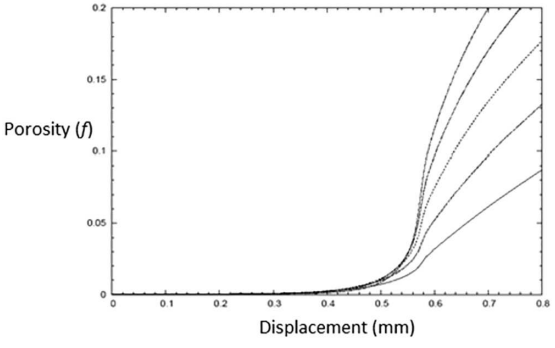

(b) LPD model with standard delocalisation

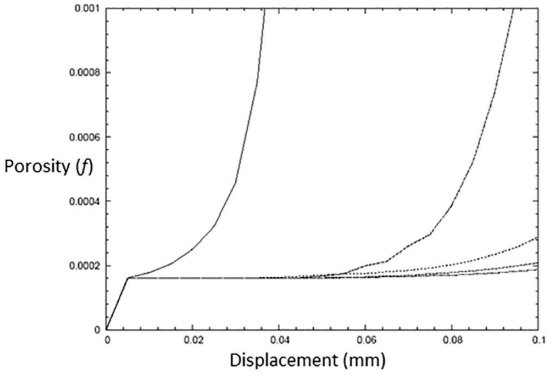

(c) LPD model with logarithmic delocalisation

Fig. 6. Porosity distribution in the meshes ahead of the crack. The distribution of porosity within the meshes ahead of the crack exhibits distinct patterns. In scenario (a), the detachment of porosity occurs gradually, Gauss point by Gauss point. Conversely, in the model with standard delocalization (b), this detachment happens at the same point. Further, in scenario (c), the detachment of porosity resumes, progressing one Gauss point after the other.

5.4. Cup-cone fracture of a round tensile specimen

The examined specimen is a meticulously designed circular cylinder characterized by an initial diameter of 30 mm and a height of 60 mm. The intentional introduction of a 1% reduction in diameter at the midpoints of the upper and lower sections, coupled with a sinusoidal variation between them, serves the specific purpose of inducing necking in the central segment of the specimen. The computational mesh, an intricate engineering construct, consists of 2070 nodes and 671 quadratic elements. Predominantly, these elements are sub-integrated quadrilaterals, complemented by a selection of triangles. Anticipating significant straining in the central region along the axis of symmetry prior to crack propagation, we strategically deploy initially flat elements in this critical area to accurately capture the intricate mechanical behavior.

In alignment with the methodology introduced by Tvergaard and Needleman [3], we model only the upper half of the specimen for computational efficiency. This bold decision dictates that the final crack deviation at 45° is achieved through a symmetrical

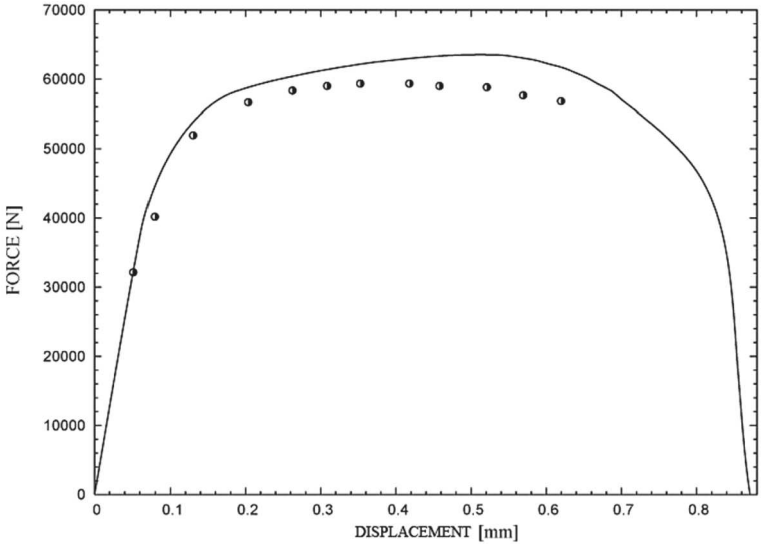

Fig. 7. Numerical predictions vs. experiments for the TA15 pre-cracked specimen.

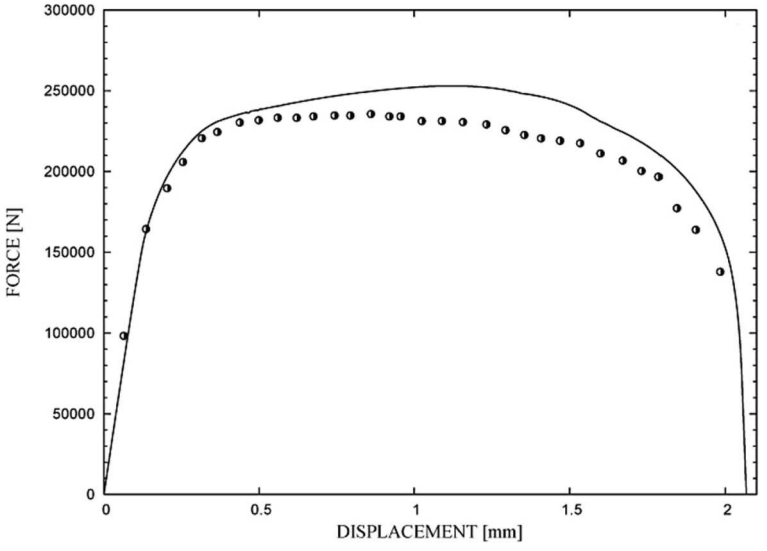

Fig. 8. Numerical predictions vs. experiments for the TA30 pre-cracked specimen.

representation about the midsection. While this modeling choice may initially appear counterintuitive from a physical standpoint, it is a calculated compromise that deliberately dismisses negligible deviations from strict symmetry. This deliberate deviation allows the crack the autonomy to "choose" either the upper or lower half of the specimen, adding nuance and flexibility to our modeling approach.

Our computational mesh, an exemplar in engineering precision, intricately combines 2070 nodes and 671 quadratic elements. These elements, predominantly sub-integrated quadrilaterals, seamlessly coalesce with a select few triangles, each contributing a unique aspect to the ensemble. In anticipation of pronounced straining within the central region along the axis of symmetry preceding pivotal crack propagation, we strategically deploy elements distinguished by exceptional flatness in this critical area. This precision ensures the faithful capture of intricate details intrinsic to the dynamic process.

In a strategic emulation of the pioneering work by Tvergaard and Needleman [3], we opt to model solely the upper hemisphere of the specimen for computational efficiency. This audacious decision dictates that the ultimate deviation of the crack at a daring 45° is orchestrated through a symphonic play of symmetry about the midpoint. While this might initially challenge conventional physical intuition, it represents a calculated compromise—a bold stance that intentionally dismisses negligible deviations from strict symmetry. This calculated risk affords the deviated crack the autonomy to "choose" either the upper or lower half of the specimen, a nuanced decision reflecting the elegance of our modeling approach. In essence, this strategic deviation from strict symmetry,

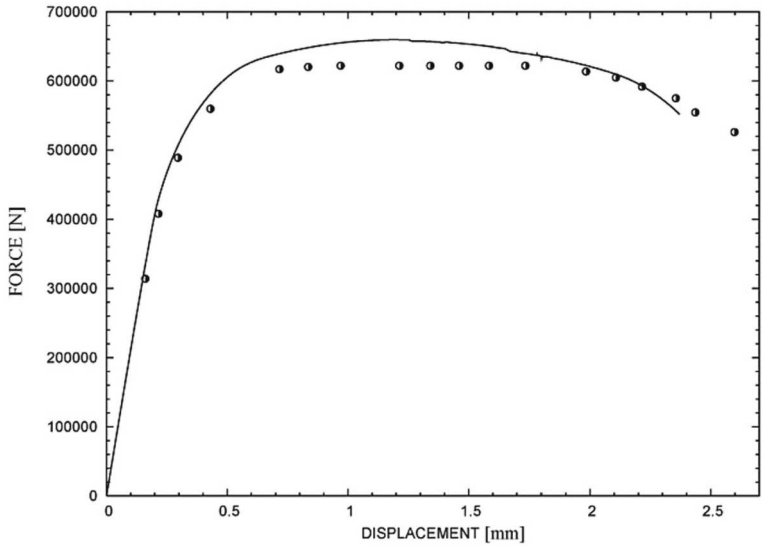

Fig. 9. Numerical predictions vs. experiments for the TA50 pre-cracked specimen.

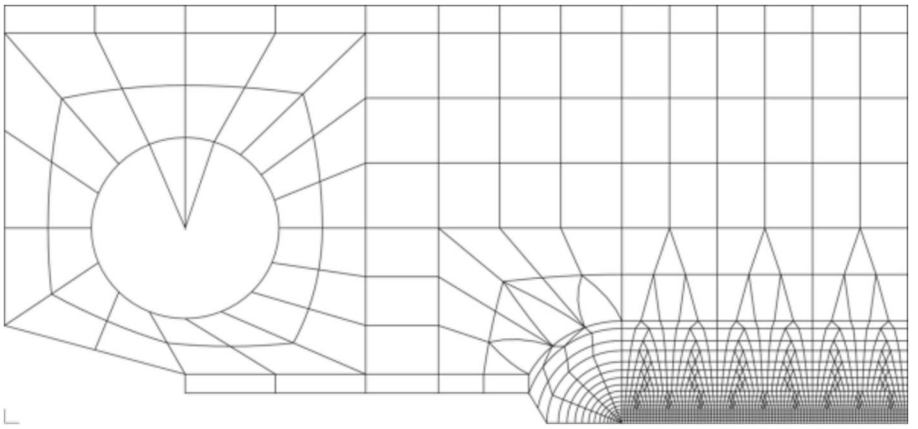

Fig. 10. Fine Mesh of the CTJ 25 pre-cracked specimen.

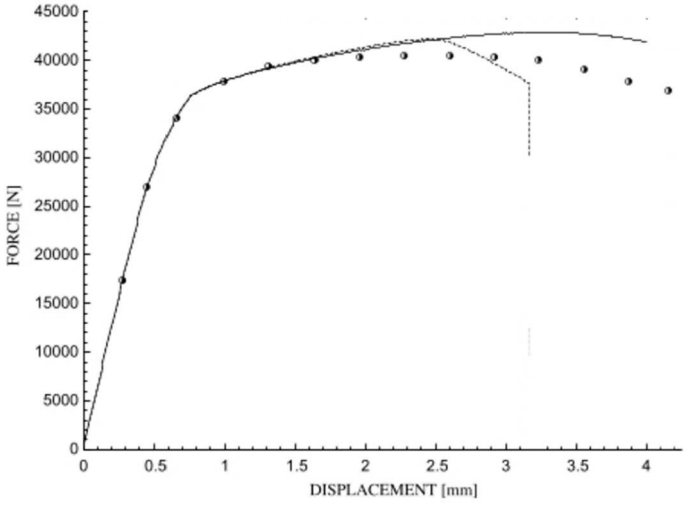

Fig. 11. Comparison of experimental and computed load–displacement curves of the CT specimen.

seemingly audacious, is a meticulously orchestrated symphony, harmonizing computational efficiency with the uncompromised portrayal of crack propagation dynamics.

The current simulation confronts formidable challenges arising from extremely sharp stress and damage gradients, introducing a subtle mesh dependency—a common intricacy encountered in ductile rupture simulations. To address this intricate issue, we adopt a sophisticated approach championed by Pijaudier-Cabot and Bazant [11], advocating the incorporation of convolution with a characteristic length approximating the void spacing into the model. This convolution, coupled with a weight function, substantiates a nonlocal quantity of paramount significance, transcending the dimensions of the void spacing.

Recent strides in simulation methodology, particularly in the context of shear banding in plane strain tension, have been achieved by adopting this convolution-based paradigm. Nevertheless, our current calculations opt for a pragmatic yet efficient strategy, diverging from convolution intricacies. Instead, we prescribe a less stringent but more straightforward approach—assigning a minimum dimension closely aligned with the void spacing to the elements. This echoes the methodology prevalent in prior works, with the minimum dimension meticulously set at 0.375 mm.

This pragmatic approach is selectively applied to elements proximate to the middle section, strategically positioned at a distance from the axis of symmetry exceeding half the specimen radius. This spatial emphasis is crucial, predicting the occurrence of non-collinear crack growth. As a consequential parametrization, the element size-to-specimen radius ratio is tightly controlled at 1/40 for these critical elements. Such precision aligns seamlessly with the counsel of Tvergaard and Needleman [3], who assert that this ratio stands sufficiently diminutive to discern the coveted cup-cone fracture phenomenon with conspicuous clarity.

The simulation unfolds in two distinct, critical stages: firstly, a relentless necking of the central specimen ensues; subsequently, a crack initiates along the axis of symmetry, relentlessly progressing towards the external surface. Crucially, the cup-cone fracture phenomenon manifests exclusively at the culmination of this second stage. Simulating this intricate phenomenon demands a substantial extension of calculations beyond the scope outlined in the preceding sections. In simulations involving void nucleation, the minimum load reached at the conclusion plummets to a mere 2.3%, virtually approaching zero. Undertaking computations entailing extensive, severely damaged, or entirely compromised regions presents formidable challenges for the convergence of the numerical algorithm. The initial dismissal of this notion was rooted in the widely accepted superiority of implicit schemes in elasto-plasticity, particularly their systematic adoption for all plasticity models.

We tackle this formidable challenge through two ingenious strategies: (i) deploying an implicit algorithm for all parameters (displacements, stresses, hardening parameters, etc.), except for softening, i.e., the porosity. This preserves compatibility with implicit schemes used for typical non-softening models; (ii) initiating iterations over the displacement increment Δu between two calculation instances t and $t + \Delta t$ with a value u extrapolated from the displacement at t and the preceding calculation. This approach ensures robust and expeditious convergence. Importantly, it obviates the need to artificially reset nodal forces in nearly failed elements to zero, a practice employed by Tvergaard and Needleman [3]; instead, the failure of successive elements occurs organically, without any user intervention.

The primary observation about the results demands attention: unequivocally, in both simulations, whether void nucleation is considered or not, the crack propagation adheres rigorously to a coplanar trajectory across the initial half of the specimen radius. This starkly contradicts the findings of Tvergaard and Needleman [3], wherein a “zig-zag” pattern was purported in the crack region. It is imperative to emphasize that this “zig-zag” pattern manifested solely within the first two rows of elements. Consequently, Tvergaard and Needleman [3] asserted that this phenomenon could not be confidently categorized as a genuine physical occurrence; instead, it might be attributable to nothing more than a mesh-induced artifact.

The velocity field within the targeted region for the anticipated cup-cone fracture phenomenon, observed in the advanced stages of the calculation without void nucleation, unequivocally demonstrates a dynamic interplay driven by the forceful sliding of two almost rigid blocks. This sliding action generates an exceptionally intense shear within the interface region, strategically oriented diagonally with respect to the loading axis. This distinct feature unequivocally points to the undeniable presence of the cup-cone fracture effect. However, a careful analysis of the velocity field at various moments reveals a significant insight: the reduction in size of the lower right zone directly results from the continuous downward and rightward motion of the interface region. This compelling observation challenges the idea of a genuine shear band formation, emphasizing that the crack maintains its steadfast propagation through the central section.

A similar conclusion can be drawn from the inspection of Fig. 12, which displays the distribution of the porosity. Indeed, though the isoporosity contours do delimit a hard (little porous) zone in the lower right region of the mesh, they demarcate no highly damaged band oriented at 45° from the loading axis, as would result from crack kinking.

The cup-cone fracture effect unequivocally remains dormant in the absence of void nucleation. Conversely, its unmistakable manifestation becomes apparent upon the inclusion of nucleation. This figure vividly captures the deformed mesh at the earliest stage of the calculation, where $A = 0.002$. The irrefutable authenticity of the observed “zig-zag” pattern within the shear band is underscored by its discernible extension spanning several rows of elements.

6. Conclusion

The paper undertakes a thorough and comprehensive examination, delving into the nuanced aspects of both the numerical implementation and assessment of Perrin’s hardening model. This exhaustive exploration spans three pivotal cases, encompassing isotropic hardening, kinematic hardening, and a hybrid approach involving both isotropic and kinematic hardening. Notably, the meticulous derivation of stiffness matrices for these models is a critical aspect, ensuring the preservation of quadratic convergence for robust numerical solutions.

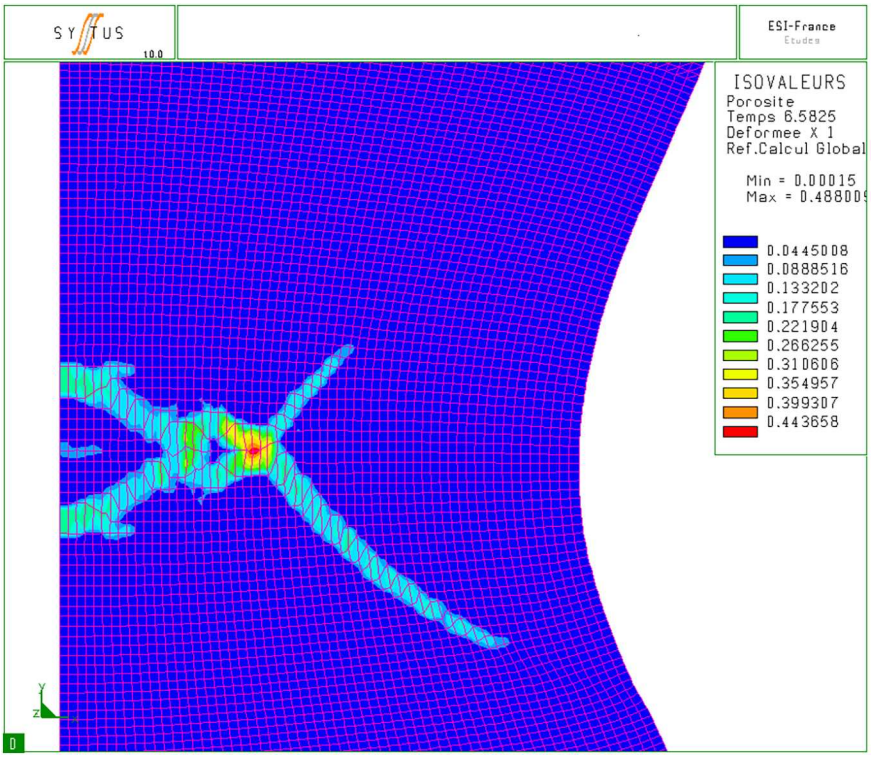

Fig. 12. Prediction of cup-cone rupture of a smooth axisymmetric specimen using the LPD model.

Moreover, the implementation goes beyond conventional constraints, accommodating large deformations to reflect real-world scenarios more accurately. This emphasis on addressing complex material behavior showcases the model's adaptability and resilience in the face of challenging conditions.

To substantiate the model's practical utility, its performance undergoes a rigorous evaluation through a meticulous comparative analysis. This analysis involves scrutinizing and contrasting experimental results with numerical simulations derived from typical ductile fracture tests. The overarching objective is to ascertain the model's effectiveness in faithfully reproducing real-world phenomena. Impressively, the comparison between experimental and numerical outcomes reveals a compelling and successful agreement, thereby highlighting the model's prowess in capturing the intricate behavior of ductile materials under static loading conditions. This substantiates the model's standing as a robust and reliable tool for understanding and predicting the behavior of materials subjected to varying degrees of stress and deformation.

In addition, the study of a cylindrical specimen's necking and crack propagation through meticulous computational modeling bolsters the paper's credibility. A strategically designed mesh adept at capturing intricate details and addressing stress gradient challenges delivers unprecedented insights. Contrary to the previous beliefs of zig-zag patterns, the simulations reveal a consistent coplanar crack propagation. The unequivocal confirmation of the cup-cone fracture effect, particularly in simulations involving void nucleation, challenges and reshapes previous interpretations. This study emphatically emphasizes the critical role of considering void nucleation for an accurate portrayal of crack propagation dynamics, reinforcing the credibility and applicability of the proposed approach in advancing the understanding of material fracture behavior.

Declaration of competing interest

The authors declare that they have no conflicts of interest to report regarding the present study.

Data availability

Data will be made available on request.

Acknowledgements

The authors wish to express their appreciation to the anonymous reviewers for their helpful suggestions which greatly improved the presentation of this paper.

The authors did not receive support from any organization for the submitted work.

Table A.2
Material parameters used for the numerical simulations on the TA and the CT specimen.

E (Mpa)	ν	Σ_0 (Mpa)	q	f_0	f_c	l (μm)	δ	A
203,000	0.3	450	1.47	0.00016	0.05	0.05	0.2	0.002

Appendix A. Material parameters for the simulations

The material parameters for the simulations presented above are shown in Table A.2.

Appendix B. Calculation of the stiffness matrices

B.1. Generalities

The objective of this section is to expose the calculation of the stiffness matrices for the classical model of ductile damage of Gurson [1], and its alternative due to Leblond-Perrin-Devaux (model LPD) [6] which have improved the modeling of the effects of work hardening in the model which are considered in this work.

Perrin [6] presents the equations of the LPD model and its numerical implementation. Analogous presentation can be found for Gurson's model in Enakoutsa et al. [8] and Enakoutsa [9]. With regard to the latter, it will therefore be essential to expose in preliminary the basic equations of the model and its numerical implementation.

The calculation of the stiffness matrix revealed a default of the numerical implementation proposed for the LPD model (and its analog for the model of Gurson). This default concerns the use, in the flow rule associated with the criterion, of a porosity $f^{\frac{1}{2}}$ at the "half-interval", i.e. at time $t+\frac{\Delta t}{2}$, during the transition from time t to time $t+\Delta t$. The purpose of introducing this porosity was to improve the numerical precision of the algorithm. Unfortunately it presents the serious disadvantage of dissymmetrizing the stiffness matrix in the case of the model of Gurson (one will not seek here to justify this assertion, which would lead us too far). We prefer a slightly different algorithm using, instead of $f'^{\frac{1}{2}}$, the final porosity (at $t+\Delta t$) f. This leads, for Gurson model, to a symmetric matrix. For the LPD model, the matrix obtained will unfortunately be asymmetrical even by taking $f^{\frac{1}{2}}=f$; we will nevertheless favor this choice for the sake of homogeneity with the numerical implementation of Gurson model.

We will not in fact calculate all the terms of the tangent-matrix but only the "most important" ones (or at least that we think so). Thus one will not take into account for the calculation of the stiffness matrix, the variation of the stresses due to the variation of the temperature; this is in fact strictly licit due to the fact that this constraint correction is carried out explicitly, using the constraints at time t and not $t+\Delta t$, and is therefore independent of the displacement increment Δu between these times. We will not take into account either the variation of the stresses due to the objective derivation in the law of hypo-elasticity, which does indeed depend on Δu and therefore theoretically generates a contribution in the tangent-matrix.

Similarly, we will not take into account the influence of the geometry on the residual forces (derivation of $\mathbf{B}$ with respect to Δu in the integral $\int_\Omega \mathbf{B}:\boldsymbol{\Sigma}\,\mathrm{dv}$). We can summarize all this by saying that the calculation of the stiffness matrix will be carried out by neglecting the effects of large transformations, that is to say by limiting ourselves to the calculation of $\partial\Sigma_{ij}\Big/\partial\Delta\varepsilon_{kl}$ where Σ denote the stress tensor at $t+\Delta t$ and $\Delta\varepsilon$ the total strain increment (elastic + plastic) between t and $t+\Delta t$. This choice is in conformity with that already made in finite element codes for the computation of the stiffness matrix for the usual models of plasticity (without damage), whose numerical experiments demonstrated the effectiveness.

B.2. Case of the Gurson model

B.2.1. New parametrization of the yield criterion and derivation

The quantities Σ_{eq},Σ_m are expressed as a function of φ and $\bar{\Sigma}$ as follows (see Eq. (85):

$$\begin{cases}\Sigma_{eq}=\bar{\Sigma}S_{eq}, S_{eq}\equiv S_{eq}(\varphi)=(1-p)cos\varphi\\ \Sigma_m=\bar{\Sigma}S_m, S_m\equiv S_m(\varphi)=\frac{2}{3}sgn(\varphi)arcosh\left[1+\frac{(1-p)^2}{2p}sin^2\varphi\right]\end{cases}\tag{B.1}$$

the derivatives of S_{eq} and S_m with respect to φ being given by

$$\begin{cases} \dfrac{dS_{eq}}{d\varphi} = -(1-p)\sin\varphi \\ \dfrac{dS_m}{d\varphi} = \dfrac{2}{3}\dfrac{(1-p)^2}{p}\dfrac{\sin\varphi\cos\varphi}{sinh\left(\frac{3}{2}S_m\right)} \end{cases} \tag{B.2}$$

B.2.2. Derivatives of $\Sigma^{*\prime}, \Sigma^*_m$ and Σ^*_{eq} with respect to $\Delta\varepsilon$

From formulas

$$\Sigma^{*\prime}_{ij} = \Sigma^{o\prime}_{ij} + 2\mu\Delta\varepsilon'_{ij}, \Delta\varepsilon'_{ij} = \Delta\varepsilon_{ij} - \frac{1}{3}\Delta\varepsilon_{kk}\delta_{ij}, \qquad \Sigma^*_m = \Sigma^o_m + (3\lambda+2\mu)\Delta\varepsilon_m = \Sigma^o_m + \frac{1}{3}(3\lambda+2\mu)\Delta\varepsilon_{kk}, \tag{B.3}$$

we draw immediately:

$$\begin{cases} \dfrac{\partial\Sigma^{*\prime}_{ij}}{\partial\Delta\varepsilon_{kl}} = 2\mu\left[\frac{1}{2}\left(\delta_{ik}\delta_{jl}+\delta_{il}\delta_{jk}\right) - \frac{1}{3}\delta_{ij}\delta_{kl}\right] \\ \dfrac{\partial\Sigma^*_m}{\partial\Delta\varepsilon_{kl}} = \dfrac{1}{3}(3\lambda+2\mu)\delta_{kl} \end{cases} \tag{B.4}$$

From Eq. (B.4), we deduce that:

$$\frac{\partial\Sigma^*_{eq}}{\partial\Delta\varepsilon_{kl}} = 3\mu\frac{\Sigma^{*\prime}_{kl}}{\Sigma^*_{eq}} \tag{B.5}$$

B.2.3. Derivatives of $\bar{\Sigma}$ with respect to $\Delta\varepsilon$ and φ

To evaluate these derivatives, we will differentiate the evolution Eq. (87) from $\Delta\bar{\varepsilon}$, written in the form:

$$(1-f)\Delta\bar{\varepsilon} = S_{eq}\Delta\varepsilon^p_{eq} + 3S_m\Delta\varepsilon^p_m = S_{eq}\frac{\Sigma^*_{eq}-\bar{\Sigma}S_{eq}}{3\mu} + 3S_m\frac{\Sigma^*_m-\bar{\Sigma}S_m}{3\lambda+2\mu} \tag{B.6}$$

Before taking this differentiation, note that:

$$\frac{dS_{eq}}{d\varphi}\Delta\varepsilon^p_{eq} + 3\frac{dS_m}{d\varphi}\Delta\varepsilon^p_m = 0; \tag{B.7}$$

this property is due to the orthogonality of $\Delta\varepsilon^p$ to the yield surface ($\boldsymbol{\Sigma} : \Delta\varepsilon^p = d\Sigma_{eq}\Delta\varepsilon^p_{eq} + 3d\Sigma_m\Delta c^p_m = 0$ if we vary Σ on the yield surface, i.e. if we vary φ, at $\bar{\Sigma}$ fixed). Given this remark, the differentiation gives:

$$(1-f)d\Delta\bar{\varepsilon} = \left(\frac{S_{eq}}{3\mu}\frac{\partial\Sigma^*_{eq}}{\partial\Delta e_{kj}} + \frac{3S_m}{3\lambda+2\mu}\frac{\partial\Sigma^*_m}{\partial\Delta\varepsilon_{kl}}\right)d\Delta\varepsilon_{kl} - \left(\frac{\Sigma_{eq}}{3\mu}\frac{dS_{eq}}{d\phi} + \frac{3\Sigma_m}{3\lambda+2\mu}\frac{dS_m}{d\phi}\right)d\phi - \left(\frac{S^2_{eq}}{3\mu} + \frac{3S^2_m}{3\lambda+2\mu}\right)\frac{d\bar{\Sigma}}{d\bar{\varepsilon}}d\Delta\bar{\varepsilon} \tag{B.8}$$

At $\varphi = const$, this gives:

$$\frac{\partial\bar{\varepsilon}}{\partial\Delta\varepsilon_{kj}} = \frac{\frac{S_{eq}}{3\mu}\frac{\partial\Sigma^*_{eq}}{\partial c_{kj}} + \frac{3S_m}{3\lambda+2\mu}\frac{\partial\Sigma^*_m}{\partial r_{kl}}}{(1-f) + \left(\frac{S^2_{eq}}{3\mu} + \frac{3S^2_m}{3\lambda+2\mu}\right)\frac{d\bar{\Sigma}}{de}} \quad \left(\text{and} \quad \frac{\partial\bar{\Sigma}}{\partial\Delta\varepsilon_{kl}} = \frac{d\bar{\Sigma}}{d\bar{\varepsilon}}\frac{\partial\Delta\bar{\varepsilon}}{\partial\Delta\varepsilon_{kl}}\right); \tag{B.9}$$

at $\Delta\varepsilon = const$, we get:

$$\frac{\partial\Delta\bar{\varepsilon}}{\partial\varphi} = -\frac{\frac{\Sigma_{eq}}{3\mu}\frac{dS_{eq}}{d\varphi} + \frac{3\Sigma_m}{3\lambda+2\mu}\frac{dS_m}{d\varphi}}{(1-f) + \left(\frac{S^2_{eq}}{3\mu} + \frac{3S^2_m}{3\lambda+2\mu}\right)\frac{d\bar{\Sigma}}{d\bar{\varepsilon}}} \quad \left(\text{and} \quad \frac{\partial\bar{\Sigma}}{\partial\varphi} = \frac{d\bar{\Sigma}}{d\bar{\varepsilon}}\frac{\partial\bar{\varepsilon}}{\partial\varphi}\right) \tag{B.10}$$

B.2.4. Derivatives of φ with respect to $\Delta\varepsilon$

It is now necessary to exploit the fundamental Eq. (90) giving φ. Note that the stresses $\Sigma_{eq^*}, \Sigma^*_m$ depend only on $\Delta\varepsilon$, while the constraints Σ_{eq}, Σ_m depend on φ and $\bar{\Sigma}$. So this equation is written as:

$$\mathcal{F}(\Delta\varepsilon, \varphi, \bar{\Sigma}) = a\left[\Sigma^*_m(\Delta\varepsilon) - \bar{\Sigma}S_m(\varphi)\right]cos\varphi - p\left[\Sigma^*_{eq}(\Delta\varepsilon) - \bar{\Sigma}S_{eq}(\varphi)\right]sinh\left[\frac{3}{2}S_m(\varphi)\right] = 0 \tag{B.11}$$

By differentiating, we get

$$\frac{\partial \mathrm{F}}{\partial \Delta\varepsilon_{\mathrm{kl}}}\mathrm{d}\Delta\varepsilon_{\mathrm{kl}} + \frac{\partial \mathrm{F}}{\partial \varphi}\mathrm{d}\varphi + \frac{\partial \mathrm{F}}{\partial \bar{\Sigma}}\mathrm{d}\bar{\Sigma} = 0, \tag{B.12}$$

where

$$\frac{\partial \mathcal{F}}{\partial \Delta\varepsilon_{\mathrm{kl}}} = \frac{\partial \mathcal{F}}{\partial \Sigma^*_{\mathrm{eq}}}\frac{\partial \Sigma^*_{\mathrm{eq}}}{\partial \Delta\varepsilon_{\mathrm{kl}}} + \frac{\partial \mathcal{F}}{\partial \Sigma^*_{m}}\frac{\partial \Sigma^*_{\mathrm{m}}}{\partial \Delta\varepsilon_{\mathrm{kl}}}, \quad \frac{\partial \mathcal{F}}{\partial \Sigma^*_{\mathrm{eq}}} = -p\,sinh\left(\frac{3}{2}\mathrm{S_m}\right), \quad \frac{\partial \mathcal{F}}{\partial \Sigma^*_{\mathrm{m}}} = a\cos\varphi, \tag{B.13}$$

$$\frac{\partial \mathcal{F}}{\partial \varphi} = p\bar{\Sigma}sinh\left(\frac{3}{2}\mathrm{S_m}\right)\frac{\mathrm{dS_{eq}}}{\mathrm{d}\varphi} - \left[a\bar{\Sigma}cos\varphi + \frac{3}{2}p\left(\Sigma^*_{\mathrm{eq}} - \Sigma_{\mathrm{eq}}\right)cosh\left(\frac{3}{2}\mathrm{S_m}\right)\right]\frac{d\mathrm{S_m}}{\mathrm{d}\varphi} - a\left(\Sigma^*_{\mathrm{m}} - \Sigma_{\mathrm{m}}\right)sin\varphi \tag{B.14}$$

$$\frac{\partial \mathcal{F}}{\partial \bar{\Sigma}} = -a\mathrm{S_m}\cos\varphi + p\mathrm{S_{eq}}sinh\left(\frac{3}{2}\mathrm{S_m}\right) \tag{B.15}$$

By expanding $d\bar{\Sigma} = \frac{\partial \bar{\Sigma}}{\partial \Delta\varepsilon_{\mathrm{kl}}}\mathrm{d}\Delta\varepsilon_{\mathrm{k}} + \frac{\partial \bar{\Sigma}}{\partial \varphi}\mathrm{d}\varphi$ in Eq. (B.12), we get:

$$\frac{\partial \mathcal{F}}{\partial \Delta\varepsilon_{\mathrm{kl}}}\mathrm{d}\Delta\varepsilon_{\mathrm{kl}} + \frac{\partial \mathcal{F}}{\partial \varphi}\mathrm{d}\varphi + \frac{\partial \mathcal{F}}{\partial \Sigma}\frac{\partial \Sigma}{\partial \Delta\varepsilon_{\mathrm{kl}}}\mathrm{d}\Delta\varepsilon_{\mathrm{k}} + \frac{\partial \mathcal{F}}{\partial \Sigma}\frac{\partial \Sigma}{\partial \varphi}\mathrm{d}\varphi = 0 \tag{B.16}$$

and thus

$$\frac{\partial \varphi}{\partial \Delta\varepsilon_{\mathrm{kl}}} = -\frac{\dfrac{\partial \mathcal{F}}{\partial \Delta\varepsilon_{\mathrm{kl}}} + \dfrac{\partial \mathcal{F}}{\partial \bar{\Sigma}}\dfrac{\partial \bar{\Sigma}}{\partial \Delta\varepsilon_{\mathrm{kl}}}}{\dfrac{\partial \mathcal{F}}{\partial \varphi} + \dfrac{\partial \mathcal{F}}{\partial \bar{\Sigma}}\dfrac{\partial \bar{\Sigma}}{\partial \varphi}}. \tag{B.17}$$

Note that the derivative $\partial\mathcal{F}\Big/\partial\varphi$ is precisely the "slope" which intervenes in Newton's method on φ used to solve Eq. (B.16).

B.2.5. Derivatives of Σ_{eq} and Σ_{m} with respect to $\Delta\varepsilon$

We have $\Sigma_{\mathrm{eq}} = \bar{\Sigma}_{\mathrm{eq}}, \bar{\Sigma}$ depending on $\Delta\varepsilon$ and φ, and $\mathrm{S_{eq}}$ of φ alone, φ being itself a function of $\Delta\varepsilon$. Therefore:

$$\frac{\partial \Sigma_{\mathrm{eq}}}{\partial \Delta\varepsilon_{\mathrm{kl}}} = \mathrm{S_{eq}}\frac{\partial \bar{\Sigma}}{\partial \Delta\varepsilon_{\mathrm{kl}}} + \mathrm{S_{eq}}\frac{\partial \bar{\Sigma}}{\partial \varphi}\frac{\partial \varphi}{\partial \Delta\varepsilon_{\mathrm{kl}}} + \bar{\Sigma}\frac{d\mathrm{S_{eq}}}{d\varphi}\frac{\partial \varphi}{\partial \Delta\varepsilon_{\mathrm{kl}}} \tag{B.18}$$

Also,

$$\frac{\partial \Sigma_{\mathrm{m}}}{\partial \Delta\varepsilon_{\mathrm{kl}}} = \mathrm{S_m}\frac{\partial \bar{\Sigma}}{\partial \Delta\varepsilon_{\mathrm{kl}}} + \mathrm{S_m}\frac{\partial \bar{\Sigma}}{\partial \varphi}\frac{\partial \varphi}{\partial \Delta\varepsilon_{\mathrm{kl}}} + \bar{\Sigma}\frac{\mathrm{S_m}}{\mathrm{d}\varphi}\frac{\partial \varphi}{\partial \Delta\varepsilon_{\mathrm{kl}}} \tag{B.19}$$

B.2.6. Derivatives of Σ' and Σ with respect to $\Delta\varepsilon$

The differentiation of the equation $\Sigma'_{\mathrm{ij}} = \dfrac{\Sigma_{\mathrm{eq}}}{\Sigma^*_{\mathrm{eq}}}\Sigma^{*\prime}_{\mathrm{ij}}$ gives

$$\frac{\partial \Sigma^*_{\mathrm{ij}}}{\partial \Delta\varepsilon_{\mathrm{kl}}} = \frac{\Sigma_{\mathrm{eq}}}{\Sigma^*_{\mathrm{eq}}}\frac{\partial \Sigma^*_{\mathrm{ij}}}{\partial \Delta\varepsilon_{\mathrm{kl}}} + \Sigma^*_{\mathrm{ij}}\left(\frac{1}{\Sigma^*_{\mathrm{eq}}}\frac{\partial \Sigma_{\mathrm{eq}}}{\partial \Delta\varepsilon_{\mathrm{k}}} - \frac{\Sigma_{\mathrm{eq}}}{\Sigma^{*2}_{\mathrm{eq}}}\frac{\partial \Sigma^*_{\mathrm{eq}}}{\partial \Delta\varepsilon_{\mathrm{kl}}}\right) \tag{B.20}$$

Finally, the equation $\Sigma_{\mathrm{ij}} = \Sigma'_{\mathrm{ij}} + \Sigma_{\mathrm{m}}\delta_{\mathrm{ij}}$ gives

$$\frac{\partial \Sigma_{\mathrm{ij}}}{\partial \Delta\varepsilon_{\mathrm{kl}}} = \frac{\partial \Sigma'_{\mathrm{ij}}}{\partial \Delta\varepsilon_{\mathrm{kl}}} + \frac{\partial \Sigma_{\mathrm{m}}}{\partial \Delta\varepsilon_{\mathrm{kl}}}\delta_{\mathrm{ij}} \tag{B.21}$$

This completes the calculation of the tangent-matrix for the Gurson's model [1].

B.3. Case of the LPD model

B.3.1. Yield locus parametrization

The stress $\Sigma_{\mathrm{eq}}, \Sigma_{\mathrm{m}}$ is expressed here as a function of φ, σ_1 and Σ_2 as follows:

$$\begin{cases} \Sigma_{\mathrm{eq}} = \Sigma_1 \mathrm{S_{eq}}(\varphi) \\ \Sigma_{\mathrm{m}} = \Sigma_2 \mathrm{S_m}(\varphi) \end{cases} \tag{B.22}$$

where the expressions for $\mathrm{S_{eq}}(\varphi)$ and $S_{\mathrm{m}}(\varphi)$, as well as their derivatives, are the same as for the Gurson model (Eq. (B.1) and Eq. (B.2))

B.3.2. Differentials of $\varepsilon_{\rm eq}$ and $\Sigma_{\rm m}$

From the equation of evolution of the hardening parameter ε_{eq}, i.e. $\dot{\varepsilon}_{\rm eq} = \dot{\varepsilon}^{\rm p}_{\rm eq}$, we deduce that

$$\varepsilon_{\rm eq} = \varepsilon^{\rm o}_{\rm eq} + \Delta\varepsilon^{\rm p}_{\rm eq} \tag{B.23}$$

$$\Rightarrow {\rm d}\varepsilon_{\rm eq} = {\rm d}\Delta\varepsilon^{\rm p}_{\rm eq} \tag{B.24}$$

Similarly, from the evolution equation $\dot{\varepsilon}_{\rm m} = \left|\dot{\varepsilon}_{\rm m}\right|$, we deduce that:

$$\varepsilon_{\rm m} = \varepsilon^{*}_{\rm m} + \left|\Delta\varepsilon^{\rm p}_{\rm m}\right| \tag{B.25}$$

$$\Rightarrow {\rm d}\varepsilon_{\rm m} = sgn\left(\Delta\varepsilon^{\rm p}_{\rm m}\right){\rm d}\Delta\varepsilon^{\rm p}_{\rm m} \tag{B.26}$$

The sign of $\Delta\varepsilon^{\rm p}_{\rm m}$ is the same as that of Σ_m, that is to say of φ according to Eq. (B.22)$_2$ and the expression of $S_{\rm m}(\varphi)$ (cf. Eq. (B.1)). Therefore

$$ {\rm d}\varepsilon_{\rm m} = \varepsilon\,{\rm d}\Delta\varepsilon^{\rm p}_{\rm m}, \quad \varepsilon = sgn(\varphi) \tag{B.27}$$

B.3.3. Derivatives of Σ_1 and Σ_2 with respect to $\Delta\varepsilon$ and φ

Let us recall that Σ_1 and Σ_2 are known, pre-tabulated functions of the hardening parameters $\varepsilon_{\rm eq}, \varepsilon_m$ (and of the initial porosity). We have:

$$d\Sigma_1 = \frac{\partial\Sigma_1}{\partial\varepsilon_{\rm eq}}{\rm d}\varepsilon_{\rm eq} + \frac{\partial\Sigma_1}{\partial\varepsilon_{\rm m}}{\rm d}\varepsilon_{\rm m} = \frac{\partial\Sigma_1}{\partial\varepsilon_{\rm eq}}{\rm d}\Delta\varepsilon_{\rm eq} + \frac{\partial\Sigma_1}{\partial\varepsilon_{\rm m}}\varepsilon{\rm d}\Delta\varepsilon^{\rm p}_{\rm m} \tag{B.28}$$

from Eq. (B.24) and Eq. (B.27). Now,

$$\Delta\varepsilon^{\rm p}_{eq} = \frac{\Sigma^{*}_{\rm eq} - \Sigma_{\rm eq}}{3\mu} = \frac{1}{3\mu}\left(\Sigma^{*}_{\rm eq} - \Sigma_1 S_{\rm eq}\right) \tag{B.29}$$

$$\Rightarrow {\rm d}\Delta\varepsilon^{\rm p}_{\rm eq} = \frac{1}{3\mu}\left(\frac{\partial\Sigma^{*}_{\rm eq}}{\partial\Delta\varepsilon_{\rm kl}}{\rm d}\Delta\varepsilon_{\rm kd} - \Sigma_1\frac{{\rm d}S_{\rm eq}}{{\rm d}\varphi}{\rm d}\varphi - S_{\rm eq}{\rm d}\Sigma_1\right) \tag{B.30}$$

Also,

$$\Delta\varepsilon^{\rm p}_{\rm m} = \frac{1}{3\lambda + 2\mu}\left(\Sigma^{*}_{\rm m} - \Sigma_2 S_{\rm m}\right) \tag{B.31}$$

$$\Rightarrow {\rm d}\Delta\varepsilon^{\rm p}_{\rm m} = \frac{1}{3\lambda + 2\mu}\left(\frac{\partial\Sigma^{*}_{\rm m}}{\partial\Delta\varepsilon_{\rm kl}}{\rm d}\Delta\varepsilon_{\rm kl} - \Sigma_2\frac{{\rm d}S_{\rm m}}{{\rm d}\varphi}{\rm d}\varphi - S_{\rm m}{\rm d}\sigma_2\right) \tag{B.32}$$

It goes without saying that the expressions of $\partial\Sigma^{*}_{\rm eq}\Big/\partial\Delta\varepsilon_{\rm kl}$ and $\partial\Sigma^{*}_{\rm m}\Big/{\rm d}\Delta\varepsilon_{\rm kJ}$ here are the same as for the Gurson model (Eq. (B.4), Eq. (B.5)). By transferring these expressions into Eq. (B.28), we obtain:

$${\rm d}\Sigma_1 = \frac{1}{3\mu}\frac{\partial\Sigma_1}{\partial\varepsilon_{\rm eq}}\left(\frac{\partial\Sigma^{*}_{\rm eq}}{\partial\Delta\varepsilon_{\rm kl}}{\rm d}\Delta\varepsilon_{\rm kl} - \Sigma_1\frac{{\rm d}S_{\rm eq}}{{\rm d}\varphi}{\rm d}\varphi - S_{\rm eq}{\rm d}\Sigma_1\right) + \frac{\varepsilon}{3\lambda + 2\mu}\frac{\partial\Sigma_1}{\partial\varepsilon_{\rm m}}\left(\frac{\partial\Sigma^{*}_{\rm m}}{\partial\Delta\varepsilon_{\rm kl}}{\rm d}\Delta\varepsilon_{\rm kl} - \Sigma_2\frac{{\rm d}S_{\rm m}}{{\rm d}\varphi}{\rm d}\varphi - S_{\rm m}{\rm d}\Sigma_2\right) \tag{B.33}$$

By reasoning in the same way for Σ_2, we obtain:

$${\rm d}\Sigma_2 = \frac{1}{3\mu}\frac{\partial\Sigma_2}{\partial\varepsilon_{\rm eq}}\left(\frac{\partial\Sigma^{*}_{\rm eq}}{\partial\Delta\varepsilon_{\rm kl}}{\rm d}\Delta\varepsilon_{\rm kl} - \Sigma_1\frac{{\rm d}S_{\rm eq}}{{\rm d}\varphi}{\rm d}\varphi - S_{\rm eq}{\rm d}\Sigma_1\right) + \frac{\varepsilon}{3\lambda + 2\mu}\frac{\partial\Sigma_2}{\partial\varepsilon_{\rm m}}\left(\frac{\partial\Sigma^{*}_{\rm m}}{\partial\Delta\varepsilon_{\rm kl}}{\rm d}\Delta\varepsilon_{\rm kl} - \Sigma_2\frac{{\rm d}S_{\rm m}}{{\rm d}\varphi}{\rm d}\varphi - S_{\rm m}{\rm d}\Sigma_2\right) \tag{B.34}$$

By successively taking $\varphi = const$ then $\Delta\varepsilon = const$ in these equations, we obtain the following two systems:

$$\begin{cases} \left(1 + \dfrac{S_{\rm eq}}{3\mu}\dfrac{\partial\Sigma_1}{\partial\varepsilon_{\rm eq}}\right)\dfrac{\partial\Sigma_1}{\partial\Delta\varepsilon_{\rm kl}} + \dfrac{\varepsilon S_{\rm m}}{3\lambda + 2\mu}\dfrac{\partial\Sigma_1}{\partial\varepsilon_{\rm m}}\dfrac{\partial\Sigma_2}{\partial\Delta\varepsilon_{\rm kl}} = \dfrac{1}{3\mu}\dfrac{\partial\Sigma_1}{\partial\varepsilon_{\rm eq}}\dfrac{\partial\Sigma^{*}_{\rm eq}}{\partial\Delta\varepsilon_{\rm kl}} + \dfrac{\varepsilon}{3\lambda + 2\mu}\dfrac{\partial\Sigma_1}{\partial\varepsilon_{\rm m}}\dfrac{\partial\Sigma^{*}_{\rm m}}{\partial\Delta\varepsilon_{\rm kl}} \\ \dfrac{S_{\rm eq}}{3\mu}\dfrac{\partial\Sigma_2}{\partial\varepsilon_{\rm eq}}\dfrac{\partial\Sigma_1}{\partial\Delta\varepsilon_{\rm kl}} + \left(1 + \dfrac{\varepsilon S_{\rm m}}{3\lambda + 2\mu}\dfrac{\partial\Sigma_2}{\partial\varepsilon_{\rm m}}\right)\dfrac{\partial\Sigma_2}{\partial\Delta\varepsilon_{\rm kl}} = \dfrac{1}{3\mu}\dfrac{\partial\Sigma_2}{\partial\varepsilon_{\rm eq}}\dfrac{\partial\Sigma^{*}_{\rm eq}}{\partial\Delta\varepsilon_{\rm kl}} + \dfrac{\varepsilon}{3\lambda + 2\mu}\dfrac{\partial\Sigma_2}{\partial\varepsilon_{\rm m}}\dfrac{\partial\Sigma^{*}_{\rm m}}{\partial\Delta\varepsilon_{\rm kl}} \end{cases} \tag{B.35}$$

$$\begin{cases} \left(1 + \dfrac{S_{\rm eq}}{3\mu}\dfrac{\partial\Sigma_1}{\partial\varepsilon_{\rm eq}}\right)\dfrac{\partial\Sigma_1}{\partial\varphi} + \dfrac{\varepsilon S_{\rm m}}{3\lambda + 2\mu}\dfrac{\partial\Sigma_1}{\partial\varepsilon_{\rm m}}\dfrac{\partial\Sigma_2}{\partial\varphi} = -\dfrac{\Sigma_1}{3\mu}\dfrac{\partial\Sigma_1}{\partial\varepsilon_{\rm eq}}\dfrac{{\rm d}S_{\rm eq}}{{\rm d}\varphi} - \dfrac{\varepsilon\Sigma_2}{3\lambda + 2\mu}\dfrac{\partial\Sigma_1}{\partial\varepsilon_{\rm m}}\dfrac{\partial S_{\rm m}}{\partial\varphi} \\ \dfrac{S_{\rm eq}}{3\mu}\dfrac{\partial\Sigma_2}{\partial\varepsilon_{\rm eq}}\dfrac{\partial\Sigma_1}{\partial\varphi} + \left(1 + \dfrac{\varepsilon S_{\rm m}}{3\lambda + 2\mu}\dfrac{\partial\Sigma_2}{\partial\varepsilon_{\rm m}}\right)\dfrac{\partial\Sigma_2}{\partial\varphi} = -\dfrac{\Sigma_1}{3\mu}\dfrac{\partial\Sigma_2}{\partial\varepsilon_{\rm eq}}\dfrac{{\rm d}S_{\rm eq}}{{\rm d}\varphi} - \dfrac{\varepsilon\Sigma_2}{3\lambda + 2\mu}\dfrac{\partial\Sigma_2}{\partial\varepsilon_{\rm m}}\dfrac{{\rm d}S_{\rm m}}{\partial\varphi}. \end{cases} \tag{B.36}$$

Solving these systems provides the value of the derivatives $\partial\Sigma_1 \Big/ \mathrm{d}\Delta\varepsilon_{kl}, \partial\Sigma_2 \Big/ \mathrm{d}\Delta\varepsilon_{kl}$, $\partial\Sigma_1 \Big/ \partial\varphi, \partial\Sigma_2 \Big/ \partial\varphi$. Note that the matrix 2×2 appearing in the first member is the same for the two systems.

B.3.4. Derivative of φ with respect to $\Delta\varepsilon$

The fundamental equation giving φ is written:

$$\mathcal{F}\left(\Delta\varepsilon,\varphi,\Sigma_1,\Sigma_2\right) = a\frac{\Sigma_2}{\Sigma_1}\left[\Sigma_m^*(\Delta\varepsilon) - \Sigma_2 \mathrm{S_m}(\varphi)\right]\cos\varphi - p\left[\Sigma_{eq}^*(\Delta\varepsilon) - \Sigma_1 \mathrm{S_{eq}}(\varphi)\right] sinh\left[\frac{3}{2}\mathrm{S_m}(\varphi)\right] = 0 \tag{B.37}$$

Its differentiation gives

$$\frac{\partial \mathrm{F}}{\partial\Delta\varepsilon_{kl}}\mathrm{d}\Delta\varepsilon_{kl} + \frac{\partial \mathrm{F}}{\partial\phi}\mathrm{d}\varphi + \frac{\partial \mathrm{F}}{\partial\Sigma_1}\mathrm{d}\Sigma_1 + \frac{\partial \mathrm{F}}{\partial\Sigma_2}\mathrm{d}\Sigma_2 = 0 \tag{B.38}$$

where

$$\frac{\partial\mathcal{F}}{\partial\Delta\varepsilon_{kl}} = \frac{\partial\mathcal{F}}{\partial\Sigma_{eq}^*}\frac{\partial\Sigma_{eq}^*}{\partial\Delta\varepsilon_{kl}} + \frac{\partial\mathcal{F}}{\partial\Sigma_m^*}\frac{\partial\Sigma_m^*}{\partial\Delta\varepsilon_{kl}}, \frac{\partial\mathcal{F}}{\partial\Sigma_{eq}^*} = -p\,sinh\left(\frac{3}{2}S_m\right), \frac{\partial\mathcal{F}}{\partial\Sigma_m^*} = a\frac{\Sigma_2}{\Sigma_1}\cos\varphi, \tag{B.39}$$

$$\frac{\partial\mathcal{F}}{\partial\varphi} = p\Sigma_1 sinh\left(\frac{3}{2}\mathrm{S_m}\right)\frac{\mathrm{dS_{eq}}}{\mathrm{d}\varphi} - \left[a\frac{\Sigma_2^2}{\Sigma_1}\cos\varphi + \frac{3}{2}p\left(\Sigma_{eq}^* - \Sigma_{eq}\right)cosh\left(\frac{3}{2}\mathrm{S_m}\right)\right]\frac{\mathrm{dS_m}}{\mathrm{d}\varphi} - a\frac{\Sigma_2}{\Sigma_1}\left(\Sigma_m^* - \Sigma_m\right)\sin\varphi, \tag{B.40}$$

$$\frac{\partial\mathcal{F}}{\partial\Sigma_1} = -a\frac{\Sigma_2}{\Sigma_1^2}\left(\Sigma_m^* - \Sigma_m\right)cos\varphi + p\mathrm{S_{eq}}\,sinh\left(\frac{3}{2}S_m\right), \frac{\partial\mathrm{F}}{\partial\Sigma_2} = \frac{a}{\Sigma_1}\left(\Sigma_m^* - 2\Sigma_m\right)cos\varphi \tag{B.41}$$

By expanding $\mathrm{d}\Sigma_1 = \frac{\partial\Sigma_1}{\partial\Delta\varepsilon_{kl}}\mathrm{d}\Delta\varepsilon_{kl} + \frac{\partial\Sigma_1}{\partial\varphi}\mathrm{d}\varphi$ and $\mathrm{d}\Sigma_2 = \frac{\partial\Sigma_2}{\partial\Delta\varepsilon_{kl}}\mathrm{d}\Delta\varepsilon_{kl} + \frac{\partial\Sigma_2}{\partial\varphi}\mathrm{d}\varphi$ in Eq. (B.38), we obtain:

$$\frac{\partial\mathcal{F}}{\partial\Delta\varepsilon_{kl}}\mathrm{d}\Delta\varepsilon_{kl} + \frac{\partial\mathcal{F}}{\partial\varphi}\mathrm{d}\varphi + \frac{\partial\mathcal{F}}{\partial\Sigma_1}\frac{\partial\Sigma_1}{\partial\Delta\varepsilon_{kl}}\mathrm{d}\Delta\varepsilon_{kl} + \frac{\partial\mathcal{F}}{\partial\Sigma_1}\frac{\partial\Sigma_1}{\partial\varphi}\mathrm{d}\varphi + \frac{\partial\mathcal{F}}{\partial\Sigma_2}\frac{\partial\Sigma_2}{\partial\Delta\varepsilon_{kl}}\mathrm{d}\Delta\varepsilon_{kl} + \frac{\partial\mathcal{F}}{\partial\Sigma_2}\frac{\partial\Sigma_2}{\partial\varphi}\mathrm{d}\varphi = 0 \tag{B.42}$$

and thus

$$\frac{\partial\varphi}{\partial\Delta\varepsilon_{kl}} = -\frac{\dfrac{\partial\mathcal{F}}{\partial\Delta\varepsilon_{kl}} + \dfrac{\partial\mathcal{F}}{\partial\Sigma_1}\dfrac{\partial\Sigma_1}{\partial\Delta\varepsilon_{kl}} + \dfrac{\partial\mathcal{F}}{\partial\Sigma_2}\dfrac{\partial\Sigma_2}{\partial\Delta\varepsilon_{kl}}}{\dfrac{\partial\mathcal{F}}{\partial\varphi} + \dfrac{\partial\mathcal{F}}{\partial\Sigma_1}\dfrac{\partial\Sigma_1}{\partial\varphi} + \dfrac{\partial\mathcal{F}}{\partial\Sigma_2}\dfrac{\partial\Sigma_2}{\partial\varphi}}. \tag{B.43}$$

Here again, we notice that $\partial\mathcal{F} \Big/ \partial\varphi$ is the "slope" used in Newton's method to solve Eq. (32).

B.3.5. Derivatives of Σ_{eq} and Σ_m with respect to $\Delta\varepsilon$

We have $\Sigma_{eq} = \bar{\Sigma}_{eq}, \bar{\Sigma}$ depending on $\Delta\varepsilon$ and φ, and $\mathrm{S_{eq}}$ of φ alone, φ being itself a function of $\Delta\varepsilon$. Therefore:

$$\frac{\partial\Sigma_{eq}}{\partial\Delta\varepsilon_{kl}} = \mathrm{S_{eq}}\frac{\partial\Sigma_1}{\partial\Delta\varepsilon_{kl}} + \mathrm{S_{eq}}\frac{\partial\Sigma_1}{\partial\varphi}\frac{\partial\varphi}{\partial\Delta\varepsilon_{kl}} + \Sigma_1\frac{d\mathrm{S_{eq}}}{d\varphi}\frac{\partial\varphi}{\partial\Delta\varepsilon_{kl}} \tag{B.44}$$

Also,

$$\frac{\partial\Sigma_m}{\partial\Delta\varepsilon_{kl}} = \mathrm{S_m}\frac{\partial\Sigma_2}{\partial\Delta\varepsilon_{kl}} + \mathrm{S_m}\frac{\partial\Sigma_2}{\partial\varphi}\frac{\partial\varphi}{\partial\Delta\varepsilon_{kl}} + \Sigma_2\frac{\mathrm{S_m}}{\mathrm{d}\varphi}\frac{\partial\varphi}{\partial\Delta\varepsilon_{kl}} \tag{B.45}$$

B.3.6. Derivatives of Σ' and Σ with respect to $\Delta\varepsilon$

The differentiation of the equation $\dot{\Sigma}'_{ij} = \frac{\Sigma_{eq}}{\Sigma_{eq}^*}\Sigma_{ij}^{*\prime}$ gives

$$\frac{\partial\Sigma_{ij}^*}{\partial\Delta\varepsilon_{kl}} = \frac{\Sigma_{eq}}{\Sigma_{eq}^*}\frac{\partial\Sigma_{ij}^*}{\partial\Delta\varepsilon_{kl}} + \Sigma_{ij}^*\left(\frac{1}{\Sigma_{eq}^*}\frac{\partial\Sigma_{eq}}{\partial\Delta\varepsilon_k} - \frac{\Sigma_{eq}}{\Sigma_{eq}^{*2}}\frac{\partial\Sigma_{eq}^*}{\partial\Delta\varepsilon_{kl}}\right) \tag{B.46}$$

Finally, the equation $\Sigma_{ij} = \Sigma'_{ij} + \Sigma_m\delta_{ij}$ gives

$$\frac{\partial\Sigma_{ij}}{\partial\Delta\varepsilon_{kl}} = \frac{\partial\Sigma'_{ij}}{\partial\Delta\varepsilon_{kl}} + \frac{\partial\Sigma_m}{\partial\Delta\varepsilon_{kl}}\delta_{ij} \tag{B.47}$$

In the two last equations, $\frac{\partial\Sigma_m}{\partial\Delta\varepsilon_{kl}}$ and $\frac{\partial\Sigma_{eq}}{\partial\Delta\varepsilon_{kl}}$ are given as in Eq. (B.44) and Eq. (B.45), terms that involved the LPD's strain hardening quantities Σ_1 and Σ_2. This completes the derivation of the stiffness matrix for the LPD's model.

References

[1] A.L. Gurson, Continuum theory of ductile rupture by void nucleation and growth: part I - yield criteria and flow rules for porous ductile media, J. Eng. Mater. Technol. 99 (1977) 2–15.
[2] V. Tvergaard, Influence of voids on shear band instabilities under plane strain conditions, Int. J. Fract. 17 (1981) 389–407.
[3] V. Tvergaard, A. Needleman, Analysis of cup-cone fracture in a round tensile bar, Acta Metall. 32 (1984) 157–169.
[4] J. Devaux, J.B. Leblond, G. Mottet, G. Perrin, Some new applications of damage models for ductile metals, in: Application of Local Fracture/Damage Models to Engineering Problems, in: Proceedings of the ASME Summer Mechanics Meeting, American Society of Mechanical Engineers, Tempe USA, 1992.
[5] J. Besson, D. Steglich, W. Brocks, Modeling of crack growth in round bars and plane strain specimens, Int. J. Solids Struct. 38 (2001) 8259–8284.
[6] G. Perrin, Contribution à l' étude théorique et numérique de la rupture ductile des métaux, Thèse de Doctorat, Ecole Polytechnique, Palaiseau, France, 1992, in French.
[7] G. Rousselier, Ductile fracture models and their potential in local approach of fracture, Nucl. Eng. Des. 105 (1) (1987) 97–111.
[8] K. Enakoutsa, J.B. Leblond, G. Perrin, Numerical implementation and assessment of a phenomenological nonlocal model of ductile rupture, Comput. Methods Appl. Mech. Eng. 196 (2007) 1946–1957.
[9] K. Enakoutsa, Modèle non-locaux en rupture ductile des métaux, Ph.D thesis, Université Pierre et Marie Curie (Paris VI), 2007, in French.
[10] K. Enakoutsa, J.B. Leblond, Numerical implementation and assessment of the GLPD micromorphic model of ductile rupture, Eur. J. Mech. A, Solids 28 (2009) 445–460.
[11] G. Pijaudier-Cabot, Z.P. Bažant, Nonlocal damage theory, J. Eng. Mech. 113 (10) (1987) 1512–1533.
[12] J.B. Leblond, G. Perrin, J. Devaux, Bifurcation effects in ductile metals with nonlocal damage, J. Appl. Mech. 61 (1994) 236–242.
[13] V. Tvergaard, A. Needleman, Effects of nonlocal damage in porous plastic solids, Int. J. Solids Struct. 32 (1995) 1063–1077.
[14] V. Tvergaard, A. Needleman, Nonlocal effects on localization in a void-sheet, Int. J. Solids Struct. 34 (1997) 2221–2238.
[15] M. Gologanu, J.B. Leblond, G. Perrin, J. Devaux, Recent extensions of Gurson's model for porous ductile metals, in: Continuum Micromechanics, vol. 377, P. Suquet (Ed.), Springer, New York, 1997, pp. 61–130.
[16] J. Mandel, Contribution theorique a l' etude de l'ecrouissage et des lois d' ecoulement plastique, in: Proceedings of the 11th International Congress on Applied Mechanics, Springer, 1964, pp. 502–509, in French.
[17] R. Hill, The essential structure of constitutive laws for metal composites and polycrystals, J. Mech. Phys. Solids 15 (2) (1967) 79–95.
[18] P. Areias, M.A. Msekh, T. Rabczuk, Damage and fracture algorithm using the screened Poisson equation and local remeshing, Eng. Fract. Mech. 158 (2016) 116–143.
[19] P. Areias, T. Rabczuk, D. Dias-da-Costa, Element-wise fracture algorithm based on rotation of edges, Eng. Fract. Mech. 110 (2013) 113–137.
[20] G. Rousselier, F. Mudry, Etude de la rupture ductile de l'acier faiblement allié en Mn-Ni-Mo pour cuves de réacteurs à eau ordinaire sous pression, approvisionné sous la forme d'une débouchure de tubulure, Résultats du programme expérimental, EdF Centre des Renardières Internal Report HT/PVD529 MAT/T43, Moret-Loing-et-Orvanne, France, 1980.
[21] F. Ahad, K. Enakoutsa, K. Solanki, D. Bammann, Nonlocal modeling in high velocity impact failure of aluminum 6160-T6, Int. J. Plast. 55 (2013) 108–132.
[22] K. Enakoutsa, Some new applications of the GLPD micromorphic model for ductile fracture, Math. Mech. Solids 19 (3) (2012) 242–259.
[23] K. Enakoutsa, K. Solanki, F. Ahad, Y. Tjiptowidjojo, D. Bammann, Using damage delocalization to model localization phenomena in Bammann-Chiesa-Johnson metals, J. Eng. Mater. Technol. 134 (4) (2012).
[24] K. Enakoutsa, K. Solanki, F. Ahad, Y. Tjiptowidjojo, D. Bammann, Damage smoothing effects in a delocalized rate sensitivity model for metals, Theor. Appl. Mech. 2 (5) (2012) 5–051005.
[25] K. Enakoutsa, An analytic benchmark solution to the problem of a generalized plane strain hollow cylinder made of micromorphic plastic porous metal and subjected to axisymmetric loading conditions, Math. Mech. Solids 20 (9) (2015) 1013–1025.
[26] K. Enakoutsa, Analytical applications and effective properties of a second gradient isotropic elastic material model, Z. Angew. Math. Phys. 66 (2015) 1277–1293.
[27] C. Fressengeas, A. Molinari, Modèle d'écrouissage cinématique en grande deformation, C.R.A.S., 297 II, 1983, p. 3.
[28] C. Fressengeas, A. Molinari, Représentation du comportement plastique anisotrope aux grandes deformations, Arch. Mech. 36 (1983) 483.
[29] J.B. Leblond, G. Perrin, Analytical study of a hollow sphere made of porous plastic material and subjected to hydrostatic tension - application to some problems in ductile fracture of metals, Int. J. Plast. 6 (1990) 677–699.
[30] J. Devaux, G. Mottet, Etude Numérique de la Rupture Ductile de l'Acier de Cuve 16MND5: Simulation des Eprouvettes Fissurées de Type TA et CTJ, Report LTSW.92/2036, ESI, Lyon, France, 1992, in French.
[31] A. Brosse, Modélisation de déchirure ductile dans un tuyau inox – Calage des paramètres de Wilkins, Report F/LE/09/042/D/BPE, ESI France Internal, Lyon, France, 2009, in French.

Highlights

- We present a numerical implementation and assessment of a model for ductile fracture, considering three hardening scenarios.
- We discuss the numerical implementation of the model and address the projection problem algorithm for three hardening.
- We introduce a numerical integration strategy for handling significant deformations and rotations in complex structures.
- We demonstrate the model effectiveness by comparing numerical simulations and experiments in pre-cracked specimens.